SCIATRAN software package (V4.6): update and further development of aerosol, clouds, surface reflectance databases and models

Linlu Mei[a,*], Vladimir Rozanov[a], Alexei Rozanov[a], John P. Burrows[a]

[a] *Institute of Environmental Physics, University of Bremen, Germany*

Abstract

Since the initiation of the development at the Institute of Environmental Physics (IUP), University of Bremen in 1994, the radiative transfer model SCIATRAN (formerly GOMETRAN) has been continuously improved and new versions have been released (Rozanov et al., 1997, 2002, 2005, 2014, 2017). In the course of development, the SCIATRAN software package became capable to simulate radiative transfer processes through the Earth's atmosphere or coupled atmosphere-ocean system with a variety of approaches to treat the sphericity of the atmosphere (plane-parallel, pseudo-spherical, approximate spherical and full spherical solutions) in both scalar and vector modes. Supported by a variety of built-in databases and parameterizations, these capabilities made SCIATRAN widely used for various remote sensing applications related to the retrieval of atmospheric trace gases and characteristics of aerosols, clouds and surface. This paper presents an overview of the clouds, aerosol and surface (CAS) databases and models implemented in the SCIATRAN software package (V4.6) and provides some recommendations on their usage. The new implementations offer potential users flexible interface to perform radiative transfer simulations: 1) accounting for multi-layer liquid water, ice and mix-phase clouds; 2) employ-

*Corresponding author
Email address: mei@iup.physik.uni-bremen.de (Linlu Mei)

ing typical aerosol type parameterizations (including vertical variability) used in satellite and model communities as well as updated databases; 3) including various surface BRDF and albedo models for land, vegetation, ocean, snow and melt ponds on sea ice.

The most recent version of the radiative transfer model SCIATRAN is freely available at the website of IUP, University of Bremen: http://www.iup.physik.uni-bremen.de/sciatran.

Keywords: SCIATRAN, Aerosol, Clouds, Surface reflectance

1. Introduction

Shortly after the beginning of space age in 1957, the first earth observation satellite flew around the Earth and discovered the Van Allen radiation belts. Since then, Earth observations satellites have been evolving and a global observation system utilising remote sensing instrumentation is now being developed. The satellite instruments have been continually evolving in the past decades. However, the explosion in the exploration of earth observation data would not have been possible without i) the simultaneous and remarkable increase in the speed of computers and their data storage and ii) the development of sofisticated forward radiative transfer models (RTMs) and retrieval algorithms.

Increasingly accurate RTMs have been developed to meet the need to simulate earth observation data from the evolving observing system. SCIATRAN, which is the subject of this paper, is a comprehensive radiative transfer software package. SCIATRAN can simulate radiative transfer processes including polarization through earth's atmosphere-ocean-land-cryosphere system in the spectral range from 175 nm to 40 μm for any observation/illumination geometries (Rozanov et al., 2014).

During the last decades, SCIATRAN became a well known and widely used radiative transfer model. The most important application areas for the SCIATRAN user community is the retrieval of atmospheric and surface parameters

using remote sensing data. Fig. 1 shows the global distribution of SCIATRAN users as of November 2022. One can see that SCIATRAN software has more than 1000 external users from 315 cities in 58 countries. By about 1400 publications (source: google scholar) the SCIATRAN software package has been cited.

Continuous developments of SCIATRAN software include two aspects: i) im-

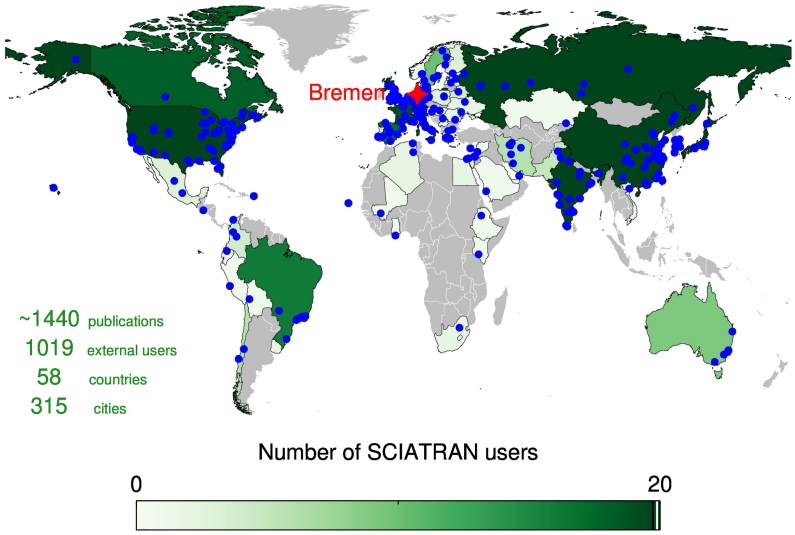

Figure 1: Geograpic distribution of SCIATRAN users worldwide as of Nov. 2022. The color indicates the total number of users in each particular country and the blue dot is the city where SCIATRAN users are located. The red star indicates city Bremen.

plementation of new features in the radiative transfer and retrieval modules; ii) update and implementation of databases and new surface reflectance models.

This paper focuses on the update of cloud & aerosol databases and implementation of new surface Bidirectional Reflectance Distribution Function (BRDF) models in the most recent SCIATRAN version - V4.6 (Rozanov et al., 2022). A comprehensive overview of the existing Cloud, Aerosol and Surface (CAS) databases and models was presented by Rozanov et al. (2014). However, a major extension of the CAS databases and models in SCIATRAN has been done after 2014. To bring the user community up to date with the options available within

SCIATRAN, this paper describes the improved cloud and aerosol databases and the usage of new surface BRDF models, available in SCIATRAN.

The paper is structured as follows. Sect. 2 contains brief information about general capabilities of the SCIATRAN software. Sect. 3 presents brief summary of the new features in SCIATRAN V4.6. In Sect. 4 we summarize new CAS databases and models implemented in SCIATRAN. Sect. 5 describes the optical properties of selected CAS. Sect. 6 shows some examples/comparisons of forward simulations using the new implementations. The conclusions are presented in Sect. 7.

2. General capabilities of the SCIATRAN software

This section gives an overview of the main features and general capabilities of the SCIATRAN software which can be of interest for potential users.

Using SCIATRAN, polarized (vector) and scalar radiative transfer calculations can be performed in plane-parallel, pseudo-spherical, approximate spherical or fully spherical geometry. Vertical inhomogeneities for parameters such as temperature, pressure, gaseous absorber concentration, aerosol particles number density, and multi-layer liquid water and ice clouds can be easily accounted for. For inexperienced users, an option of a vertically homogeneous medium, which requires minimum number of input parameters, might be useful.

The surface reflection can be described as 1) wavelength dependent Lambertian reflection or constant albedo; 2) BRDF including parameterizations for a variety of surface types (ocean, vegetation, soil, snow, melt ponds and sea ice). In particular, in the case of light reflection by an ocean surface, the SCIATRAN software enables to consider the Fresnel reflection from absolutely calm and wind-roughed surface (accounting for polarization), whitecap reflection, and water leaving radiation. Reflection by white ice and melt ponds on sea ice can also be accounted for. In addition, a coupled ocean-ice-atmosphere system can be considered to simulate the radiative transfer over and under the ice/water

surface.

The software package has been designed to perform fast and accurate simulations of radiance spectra appropriate to atmospheric remote sensing observations in the UV-VIS-NIR-SWIR-TIR spectral ranges. Different models and databases included in SCIATRAN are valid in different spectral ranges. In the spectral range 225 – 2500 nm, most of the described database can be used. Generally, the calculations can be performed in the spectral range from 175.44 nm to 40 μm, including O_2 Schumann-Runge and Herzberg absorption bands in UV spectral range, various gaseous absorbers such as O_3, NO_2, CIO, OCIO, BrO, HCHO, SO_2, NO_3, O_4, O_2, H_2O, CO_2, CO, CH_4, N_2O throughout the whole spectral range and thermal emission in the TIR spectral range. Depending on the spectral range, some limitations in the functionality might apply.

All relevant elastic scattering processes such as the Rayleigh scattering, aerosol and cloud scattering & absorption can be taken into account. Additionally, important inelastic scattering processes such as vibrational Raman scattering and Colored Dissolved Organic Matter (CDOM) fluorescence in the ocean (Rozanov et al., 2017, Wolanin et al., 2015), the rotational Raman scattering in the atmosphere (including electron spin-rotational splitting) (Rozanov and Vountas, 2013, Lelli et al., 2017, Rozanov et al., 2021), can be accounted for. SCIATRAN also includes a retrieval block, which enables a continually increasing number of earth observation data products from ground based, ship, aircraft or satellite borne sensors to be delivered in near real-time. This block, however, is not a part of the freely distributed software package.

Employing the SCIATRAN software, users can calculate radiance/intensity (scalar mode) or Stokes vector (vector mode), scalar or vector weighting functions (Jacobian matrix) for concentrations of gaseous absorbers, cloud optical thickness, cloud top and bottom heights, effective radius of water droplets and ice crystals, aerosol number density, surface albedo and many other parameters. [1] Air mass factors (AMF), slant columns, vertically resolved AMFs (box AMFs),

[1] A complete list of all available parameters can be found in the SCIATRAN user guide

fluxes (actinic, upwelling, downwelling, diffuse and total), spherical albedo, diffuse transmission, vertical optical depth. Such characteristics of radiation field as fluxes, spherical albedo, and diffuse transmission can also be calculated assuming specific isotropic illumination conditions of a medium from above and below.

The SCIATRAN software contains not only different solvers (stand along discrete-ordinates method (DOM) (Siewert, 2000), combined differential-integral (CDI) approach (Rozanov et al., 2000) initialized by either DOM or finite difference method (FDM) (Barkstrom, 1976), and CDI approach involving the Picard iterative approximation (Rozanov et al., 2001) initialized by either DOM or FDM solution.) , which are capable to perform radiative transfer calculations through a plane-parallel or spherical atmosphere but also numerous parameterizations of the Rayleigh scattering, databases of aerosol and cloud optical properties as well as various models of the surface BRDF, which significantly facilitate the usage of software especially for novice users. Taking into account that parameterizations of the Rayleigh scattering have been discussed in Rozanov et al. (2014), following sections will present newly implemented databases of aerosol and cloud optical properties as well as models of the bidirectional surface reflection. A consideration of databases for numerous gaseous absorber including HITRAN 2020 molecular spectroscopic database (Gordon et al., 2022) is out of scope of this paper.

3. Overview of new SCIATRAN features

While the initial development of SCIATRAN was dedicated to the satellite missions GOME (Global Ozone Monitoring Experiment) and SCIAMACHY (SCanning Imaging Absorption spectroMeter for Atmospheric CHartography) and their products (Burrows et al., 1995, Bovensmann et al., 2010, Buchwitz et al., 2013, Richter et al., 2005, Noël et al., 2018, Arosio et al., 2018, Weber et al., 2018), the implementation of CAS databases and models in SCIATRAN

is mainly driven by the developments of the eXtensible Bremen Aerosol/cloud and surfacE parameters Retrieval (XBAER) algorithm and its products. The XBAER algorithm is now capable to provide global data products for clouds (Mei et al., 2017b, 2018a, 2019), aerosol (Mei et al., 2017a, 2018b, 2020a,b) and surface parameters (Mei et al., 2021a,b). The further developments of SCIATRAN support 1) the design of new instruments (e.g., Carbon Monitoring Satellite (CarbonSat) (Buchwitz et al., 2013), Methane Airborne MAPper (MAMAP) (Gerilowski et al., 2011)); 2) the release of new versions of atmospheric and surface satellite products in Institute of Environmental Physics (IUP), University of Bremen; 3) the exploration of new applications for related research topics worldwide.

Table 1 summarizes new implementations of CAS since the paper of Rozanov et al. (2014). All CAS databases and models from the previous versions of SCIATRAN are still available in V4.6. In particular, 1) cloud databases include liquid water clouds with effective radius of water droplets in the range 4 – 20 µm, and ice clouds consisting of ice crystals having the shape of second generation fractal; 2) aerosol databases include OPAC version 3, WMO and LOWTRAN; 3) models for surface BRDF are RPV, modified RPV, and RTLSR. In V4.6, optical characteristics of liquid water cloud database have been extended to cover the water droplet effective radii between 2 - 40 μm in contrast to 4 - 20 μm in the previous version. The Baum (Baum et al., 2011) and Yang (Yang et al., 2013) ice crystal databases have been included in SCIATRAN. Many important details of the Yang database implementation can be found in Pohl et al. (2020). Aerosol type parameterizations such as Moderate Resolution Imaging Spectroradiometer (MODIS) Dark-Target (DT) over land (Levy et al., 2013) and ocean (Remer et al., 2005), Modern-Era Retrospective analysis for Research and Applications (MERRA) (Randles et al., 2017), and XBAER (Mei et al., 2017a) have been implemented. In addtion, the updated Optical Properties of Aerosols and Clouds (OPAC) dataset (Köpke et al., 2015) and optical parameters of dust aerosol particles according to Dubovik et al. (2006) have also implemented.

The XBAER surface reflectance parameterization (Mei et al., 2017a), RossThick-

Table 1: Databases and models described in (Rozanov et al., 2014) and in this paper

Paper	Rozanov et al. (2014)	This paper
Cloud	liquid water and ice clouds	update of liquid water and ice clouds
Aerosol	OPAC 3, WMO, LOWTRAN	OPAC 4, MERRA, XBAER, MODIS Dark-Target, spheroidal dust
Surface	RPV, modified RPV (mRPV) mRPV plus facet, RTLSR	XBAER, FASMAR, RTLSRS, snow and melt ponds on sea ice

LiSparseReciprocal-Snow (RTLSRS) (Jiao et al., 2019), Fast and Accurate Semi-analysical Model of Atmosphere-surface Reflectance (FASMAR) (Mei et al., 2022), and BRDF models for snow, white ice and melt ponds on sea ice are now available.

In recent years, to address the exponentially increasing amount of remote sensing data, fast radiative transfer models focused on specific data products have been developed. Examples are i) FASMAR (Fast and Accurate Semi-analytical Model of Atmosphere and Surface Reflectance (Mei et al., 2022) is used with XBAER to retrieve surface (e.g., snow grain size, specific surface area) and aerosol products (e.g., AOT); ii) FOCAL: Fast atmOspheric traCe gAs retrievaL (Reuter et al., 2017) uses a simplified RTM to determine the dry mole fractions of carbon dioxide, XCO_2, and methane, XCH_4, from measurements of the radiance in the Near Infrared, NIR, and Short-wave Infrared, SWIR. These models have also benefited from SCIATRAN, in its being a high accuracy reference RTM.

4. CAS databases and models implemented in SCIATRAN

In this section, we briefly introduce the CAS databases and models newly implemented in SCIATRAN. Almost all databases can be used to perform radiative transfer simulations in the spectral range at least between 225 nm and 2.5 μm.

4.1. Aerosol

In our seminal paper (Rozanov et al., 2014) dedicated to the software package SCIATRAN such aerosol models and databases as World Meteorological Organization (WMO) (Bolle, 1986), LOWTRAN (Levoni et al., 1997) and OPAC version 3 (Hess et al., 1998) have been described. We recall that WMO and LOWTRAN databases contain optical characteristics (extinction coefficient, single scattering albedo and scattering matrix (or phase function in the scalar case)) of different aerosol components and aerosol types, respectively. In particular, in the WMO database six aerosol components are included, namely water soluble, dust, oceanic, soot, stratospheric and volcanic. The commonly used aerosol types (e.g., continental, maritime, urban) are defined by the external mixture of the optical properties of those six components. The user has to specify the vertical profile of the aerosol extinction coefficient at a reference wavelength.

The LOWTRAN database (version 7) consists of extinction and scattering coefficients and asymmetry parameters for pre-defined aerosol types located in different atmospheric layers (i.e., boundary layer, troposphere, stratosphere and mesosphere). The basic aerosol types in boundary layer include rural, urban and maritime aerosols. Only one type is available for the tropospheric aerosols. For both boundary layer and the troposphere, the humidity and visibility is to be selected by the users. In the stratosphere, users can select 1) either background or volcanic (moderate, high, extreme) aerosol loading; 2) either fresh or aged volcanic aerosol type. For the mesosphere a choice between normal aerosol state and a transition from the volcanic stratosphere to the normal mesosphere is available.

The OPAC (version 3) database (Hess et al., 1998) implemented into the SCIATRAN software consists of refractive indices and parameters of log-normal particle size distribution functions of predefined components such as insoluble, meteoritic dust, mineral (nuc., acc., coa., mode), mineral-transported, soot, sulfate, sea salt (acc., coa. mode), and water soluble. The optical properties of an aerosol type are calculated as the external mixture of predefined aerosol com-

ponents using the Mie code published by Mishchenko et al. (1999), which is incorporated in SCIATRAN. The calculation of optical characteristics is performed automatically by the SCIATRAN software without any further actions by users if option OPAC is selected.

The following new aerosol databases have been implemented in the recent SCIATRAN version: an updated OPAC database, MODIS Dark-Target (both land and ocean), MERRA, XBAER, and Dust aerosol types. These aerosol types provide aerosol parameterization methods, which are well-received by the aerosol community.

When selecting a suitable aerosol database or parameterization, beside the requirement with respect to the appropriate spectral range, a possibility to use altitude dependent particle number density and optical properties (extinction cross-section, Single Scattering Albedo (SSA) and phase function) is also an important issue. In contrast to the aerosol particle number density, which can be defined as a function of altitude, for all newly implemented aerosol types in SCIATRAN, altitude dependent particle optical properties can only be defined when using MERRA or OPAC aerosol types. We note that SCIATRAN users can define a specific altitude-dependent aerosol type using OPAC micro-physical properties. However, the usage of MERRA types is significantly simpler as compared to OPAC, because it does not require from user any a priori knowledge about chemical composition and micro-physical properties of aerosol types in different atmospheric layers. The aerosol types which were available in previous SCIATRAN version (e.g., WMO and LOWTRAN) enable the users to describe the altitude dependent optical properties only for pre-defined altitude layers (boundary layer, troposphere, stratosphere, and mesosphere). The newly implemented MODIS Dark-Target, XBAER, and Dust aerosol parameterizations define altitude independent aerosol types.

4.1.1. OPAC aerosol type

In the previous version of SCIATRAN paper (Rozanov et al., 2014), the details of OPAC version 3 database (Hess et al., 1998) have been described. A new version of OPAC (version 4.0) was released recently by Köpke et al. (2015). The main improvement is the update of shape of mineral dust, from spherical to prolate spheroids. The usage of a spherical assumption for dust particles was proven to introduce large errors for both aerosol properties retrieval (Zhao et al., 2003) and dust radiative forcing calculations (Mishchenko, 2001). The usage of the OPAC (version 4.0) database within the SCIATRAN software does not require Mie calculations because the database includes phase functions at discrete number of scattering angles and extinction and scattering coefficients pre-calculated employing T-matrix and geometric optics methods (Köpke et al., 2015).

4.1.2. MODIS Dark-Target aerosol types

The MODIS-DT aerosol type is operationally used to derive NASA aerosol properties dataset from MODIS and Visible Infrared Imaging Radiometer Suite (VIIRS) instruments (Levy et al., 2013, Remer et al., 2020). This aerosol type provides an aerosol parameterization method, which is well-received by the aerosol community.

The MODIS dark-target aerosol type parameterization is different for aerosols over the land and ocean.

Dark-Target aerosol type over land (MODIS-DT).

The MODIS-DT aerosol parameterization implemented into the SCIATRAN software offers the following aerosol types: Weakly Absorbing (WA), Moderately Absorbing (MA), Strongly Absorbing (SA), and specific spheroidal (dust). Although the continental aerosol type was also included in the original MODIS Dark-Target over land aerosol parameterization, this type is not included in the current SCIATRAN database because 1) the continental aerosol type is used only when none of the three aerosol types (WA, MA and SA) can provide sat-

isfactory retrieval results in the Dark-Target algorithm for MODIS instrument (personal communication with Dr.Robert Levy); 2) this type is not used in the XBAER algorithm as it was found by us to provide unsatisfactory results for MERIS instrument.

Each aerosol type contains fine and coarse modes (hereafter mode 1 and 2), which are characterized by the volume PSD given by

$$\frac{dV}{d\ln r} = \frac{V_0}{\sqrt{2\pi}\,\sigma}\exp\left[-\frac{(\ln r - \ln r_v)^2}{2\sigma^2}\right], \quad (1)$$

where V_0 is the total volume of particles in a vertical column of a unit area, r_v is the mode radius and σ is the standard deviation. Parameters of the aerosol Particle Size Distribution (PSD) function and the Refractive Index (RI) for each mode are represented as functions of the Aerosol Optical Thickness (AOT) at the wavelength of 0.55 μm. The parameterization formulas for each aerosol type and mode are listed in Table 2. We note that the relationships presented in the table are valid for $\tau \leq 2$ for MA and SA types and for $\tau \leq 1$ for WA and dust types. For larger values of τ, $\tau = 2$ and $\tau = 1$, respectively, is to be used in the formulas.

For selected aerosol type and AOT, SCIATRAN calculates parameters of the volume PSD and RI for the fine and coarse modes according to Table 2. Then, employing incorporated Mie code, the scattering and absorption cross-sections as well as the scattering matrix are calculated. The optical parameters for the selected aerosol type are calculated thereafter as follows

$$\sigma_p = f\,\sigma_{p_1} + (1-f)\,\sigma_{p_2}\ , \quad (2)$$

where subscript "p" denotes scattering "s", absorption "a" or extinction "e" cross-section and f is the fraction of fine mode given by $f = N_{01}/(N_{01}+N_{02})$. To calculate the fine mode fraction, the following relationship between the total volume, V_0, and the total particle number in a vertical column of a unit area, N_0, is employed

$$N_0 = V_0\,\frac{3}{4\pi r_v^3}\exp\left(\frac{9\sigma^2}{2}\right)\ . \quad (3)$$

Table 2: Parameters of PSD function and refractive indices of DT-land aerosol types according to Levy et al. (2007).

Type	Mode	r_v (μm)	σ	V_0 ($\mu m^3/\mu m^2$)	Refractive Index
Moderately	1	$0.0203\tau+0.145$	$0.1365\tau+0.3738$	$0.1642\tau^{0.7747}$	$1.43-(0.002\tau+0.008)\,i$
absorbing	2	$0.3364\tau+3.101$	$0.098\tau+0.7292$	$0.1482\tau^{0.6846}$	$1.43-(0.002\tau+0.008)\,i$
Weakly	1	$0.0434\tau+0.1604$	$0.1529\tau+0.3642$	$0.1718\tau^{0.8213}$	$1.42-(0.0015\tau+0.007)\,i$
absorbing	2	$0.1411\tau+3.3252$	$0.1638\tau+0.7595$	$0.0934\tau^{0.6394}$	$1.42-(0.0015\tau+0.007)\,i$
Strongly	1	$0.0096\tau+0.1335$	$0.0794\tau+0.3834$	$0.1748\tau^{0.8914}$	$1.51-0.02\,i$
absorbing	2	$0.9489\tau+3.4479$	$0.0409\tau+0.7433$	$0.103\tau^{0.6824}$	$1.51-0.02\,i$
Spheroidal	1	$0.1416\tau^{-0.0519}$	$0.7561\tau^{0.148}$	$0.0871\tau^{1.026}$	$1.48\,\tau^{-0.021}$ - $0.0025\tau^{0.132}\,i$ (0.47)
(dust)					$1.48\,\tau^{-0.021}$ - $0.002\,i$ (0.55)
					$1.48\,\tau^{-0.021}$ - $0.0018\tau^{-0.08}\,i$ (0.66)
					$1.46\,\tau^{-0.040}$ - $0.0018\tau^{-0.30}\,i$ (2.1)
	2	2.2	$0.554\tau^{-0.0519}$	$0.6786\tau^{1.0569}$	the same as for Mode 1

The phase function is calculated as

$$p(\gamma) = \frac{\sigma_{s_1}\, p_1(\gamma) + \sigma_{s_2}\, p_2(\gamma)}{\sigma_s} \,, \tag{4}$$

where γ is the scattering angle.

The usage of MODIS-DT aerosol type parameterization within SCIATRAN software requires the user to select one of the above discussed aerosol types and to provide AOT at the wavelength of 0.55 μm. In addition, the user can define any shape, $S_h(z)$, of the aerosol number density vertical distribution (the default shape is a constant within an aerosol layer). The number density profile is then calculated as

$$N(z) = \frac{\tau}{\sigma_e \int\limits_0^H S_h(z)\, dz}\, S_h(z) \,, \tag{5}$$

where H is the top height of the aerosol layer. In the operational MODIS-DT aerosol product, the aerosol layer is assumed to be located between 0 - 3 km with an exponential number density vertical distribution.

MODIS-DT aerosol types were used in the framework of SCIATRAN software to calculate the lookup tables widely used in the AOT retrieval algorithm over land (Mei et al., 2017a, 2020b).

Table 3: Parameters of PSD function and refractive indices of DT-ocean aerosol fine and coarse modes according to Remer et al. (2005). Details of the table below can be found on https://darktarget.gsfc.nasa.gov/algorithm/ocean/aerosol-models

Mode	r_g	σ	RI(0.466 - 0.857μm)	RI(1.241μm)	RI(1.628μm)	RI(2.113μm)
F1	0.07	0.4	1.45-0.0035i	1.45-0.0035i	1.45-0.01i	1.40-0.005i
F2	0.06	0.6	1.45-0.0035i	1.45-0.0035i	1.45-0.01i	1.40-0.005i
F3	0.08	0.6	1.40-0.0020i	1.40-0.0020i	1.39-0.005i	1.36-0.003i
F4	0.10	0.6	1.40-0.0020i	1.40-0.0020i	1.39-0.005i	1.36-0.003i
C1	0.40	0.6	1.35-0.001i	1.35-0.001i	1.35-0.001i	1.35-0.001i
C2	0.60	0.6	1.35-0.001i	1.35-0.001i	1.35-0.001i	1.35-0.001i
C3	0.80	0.6	1.35-0.001i	1.35-0.001i	1.35-0.001i	1.35-0.001i
C4	0.60	0.6	1.53-0.003 i (0.47) 1.53-0.001i (0.55) 1.53-0.000i (0.65) 1.53-0.000i (0.86)	1.46-0.000i	1.46-0.001i	1.46-0.000i
C5	0.50	0.8	the same as for Mode C4	1.46-0.000i	1.46-0.001i	1.46-0.000i

Dark-Target aerosol type over ocean (MODIS-OC).

Unlike the land case, the aerosol type over the ocean in the DT algorithm is defined by selecting one of the four fine modes (F1, F2, F3, F4) and one of the five coarse modes (C1, C2, C3, C4, C5). The PSD parameters and RI are given in Table 3. For wavelengths selected by users, the Mie code is used by the SCIATRAN software to calculate scattering and extinction cross-sections as well as scattering matrices. The fine mode, coarse mode, and the fraction of coarse mode are input parameters. In contrast to the MODIS-DT aerosol type, which requires AOT as an input parameter, a vertical profile of the aerosol particles number density in physical units needs to be provided over ocean. Using the calculated extinction cross-section and number density profile, AOT is calculated and written out by the SCIATRAN software.

4.1.3. XBAER aerosol type over ocean (XBAER-OC)

The XBAER aerosol type was originally designed for the usage within the framework of the XBAER retrieval algorithm. A similar strategy, as described by Levy et al. (2007), has been employed to obtain aerosol types over the ocean. In particular, the statistical analysis was performed using the Maritime Aerosol Network (MAN) observations (Smirnov et al., 2009) and four aerosol types, namely pure maritime, pollution 1, pollution 2 and dust influenced were defined. Table 4 shows the volume PSD parameters and RI of these predefined aerosol types as used in the XBAER algorithm over ocean and implemented into the SCIATRAN software.

A slight difference as compared to the MODIS-DT aerosol types is that the XBAER ocean aerosol type is parameterized not only with respect to AOT at $0.55\,\mu$m, τ, but also with respect to fine-mode AOT at $0.55\,\mu$m, τ_f. The fine-mode AOT is defined as the product of the total AOT at $0.55\,\mu$m and fine mode volume fraction, which is also a function of τ. The fine mode volume fraction is calculated as $f_v = V_{01}/(V_{01} + V_{02})$, where V_{01} and V_{02} are given in Table 4 as function of τ for mode 1 and 2, respectively.

The input parameters for this parameterization are the aerosol type (pure maritime, pollution 1, pollution 2 or dust influenced), AOT at $0.55\,\mu$m, and the shape of the aerosol number density profile similarly to MODIS-DT aerosol type over land.

A combination of MODIS-DT for land and XBAER-OC for ocean aerosol types enable the same treatment of global aerosol prameterization. For a given location and time, a unique aerosol type can be selected and used for global aerosol retrieval over land and ocean (Mei et al., 2017a, 2018a). The XBAER aerosol type is operationally used to derive ESA Climate Change Initiative (CCI) and Copernicus Climate Change Service (C3S) aerosol properties dataset from MEdium Resolution Imaging Spectrometer (MERIS) and Ocean and Land Colour Instrument (OLCI) instruments using lookup table calculated with SCIATRAN software (Mei et al., 2017a, 2018b).

Table 4: Parameters of PSD function and refractive index of XBAER-ocean aerosol types according to Mei et al. (2018b).

Type	Mode	r_v (μm)	σ	V_0 ($\mu m^3/\mu m^2$)	Refractive Index
Pure Maritime	1	$0.115\tau_f{}^{-0.05}$	$0.42\tau_f{}^{-0.02}$	0.078τ	1.415-0.002i
	2	$1.376\tau_f{}^{-0.06}$	$0.732\tau_f{}^{0.016}$	0.588τ+0.002	1.363-3 10^{-9} i
Pollution 1	1	0.042τ+0.137	$0.435\tau_f{}^{0.076}$	0.144τ+0.009	1.48+0.053τ-(-0.002τ+0.006)i
(Organic/black carbon)	2	1.122τ+1.528	$0.658\tau_f{}^{-0.05}$	$0.059\tau^{-0.18}$	1.48+0.053τ-(-0.002τ+0.006)i
Pollution 2	1	0.053τ+0.144	$0.499\tau^{0.092}$	0.141τ+0.015	1.419+0.037τ-(-0.002τ+0.005)i
(Sulfates)	2	0.31τ+2.195	$0.6\tau^{-0.06}$	0.115τ+0.018	1.419+0.037τ-(-0.002τ+0.005)i
Dust influenced	1	0.048τ+0.117	$0.556\tau_f{}^{-0.03}$	0.035τ+0.01	$0.0025\tau^{0.132}$
(dust)	2	$0.072\tau_f$+1.622	$0.531\tau^{-0.08}$	$0.617\tau^{1.15}$	$0.0025\tau^{0.132}$

4.1.4. Dubovik dust aerosol type

Dust aerosol is a very important aerosol type. Many investigations have been done specifically for the dust aerosol. For example, compared to OPAC version 3.0, the OPAC version 4.0 mainly improves the treatment of the dust. In the MODIS-DT aerosol type, the spheroidal dust can also be used. However, the online calculation of the aerosol optical parameters in the case of non-spherical particles is usually very time consuming. To reduce the calculation time, the pre-calculated kernel look-up-tables and software to calculate optical parameters of dust aerosol type were presented by Dubovik et al. (2006). This software package is not yet included in SCIATRAN, but SCIATRAN is capable to read optical parameters of dust aerosol calculated externally employing the kernels look-up-table. Thus, the input parameters for this aerosol type are pre-calculated optical parameters, AOT at selected wavelengths, and the aerosol number density profile.

The Dubovik dust aerosol type is operationally used to derive ESA Climate Change Initiative (CCI) aerosol properties dataset from Polarization and Anisotropy of Reflectances for Atmospheric science coupled with Observations from a Lidar (PARASOL) (Dubovik et al., 2014).

This aerosol type was also used to calculate the TOA reflectance of aerosol contaminated clouds using SCIATRAN software and to support the derivation of

AOT above cloud over western Africa (Mei et al., 2019). Moreover, a possibility to combine the dust aerosol type with other aerosol types (e.g., WMO type) implemented in SCIATRAN was successfully demonstrated by Mei et al. (2019). The full release of this new implementation will be included in the upcoming SCIATRAN version.

4.1.5. MERRA aerosol type

A mismatch between the satellite-derived and model-simulated aerosol properties exists due to different treatments of aerosol types in satellite and model communities. In fact, aerosol type and corresponding optical properties in model community typically depend on time, geographic location, and altitude, whereas the dependence of aerosol type on the altitude is not accounted for in satellite community. To minimize this mismatch, we proposed a new global aerosol type parameterization for the XBAER algorithm, which characterizes aerosol type parameterization uses the aerosol optical properties based on the MERRA aerosol components. As the first step these components are included in the SCIATRAN software.

The MERRA model contains 15 aerosol tracers (components): sulfate (SU), hydrophobic and hydrophilic modes of organic carbon (OC) and black carbon (BC) aerosol, and five non-interacting size bins for dust (DU) and sea salt (SS) aerosol (see Table 5). Each aerosol component is defined by a fixed size distribution. In particular, the size distributions for SU, OC, and BC components are described by a lognormal distribution function. The optical database for each tracer, i, includes extinction, Q_{ei}, and scattering, Q_{si}, efficiency and expansion coefficients of scattering matrix elements pre-calculated at predefined wavelength and humidity grids. Additionally, the database includes cross sectional area, A_i, and particle mass, m_i, at predefined humidity grids.

The extinction cross-section is calculated as

$$\sigma_{ei}(\lambda, h) = Q_{ei}(\lambda, h)\, A_i(h)\, m_i(0)\ , \tag{6}$$

where h is the humidity and $m_i(0)$ is the dry mass of tracer i, $i = 1, 2, \ldots, 15$. Here and thereafter, cross sectional area, A_i, is given per kg dry mass. Replacing $Q_{ei}(\lambda, h)$ in Eq. (6) with $Q_{si}(\lambda, h)$, the scattering cross-section, $\sigma_{si}(\lambda, h)$, for tracer i is obtained.

In order to calculate the extinction coefficient one needs to calculate tracer number density

$$N_i(z) = \frac{r_i(z)\,\rho_{air}(z)}{m_i(0)}\ , \tag{7}$$

where $r_i(z)$ is the mass-mixing ratio for the dry air, $\rho_{air}(z)$ is the air density and z is the altitude. The air density and mass-mixing ratio for all tracers are obtained from the MERRA input data file. The extinction coefficient of tracer i is given by

$$e_i(\lambda, z) \ = \ \sigma_{ei}(\lambda, h_z)\, N_i(z)\ , \tag{8}$$

and the extinction coefficient of MERRA aerosol type is

$$e(\lambda, z) \ = \ \sum_{i=1}^{15} \sigma_{ei}(\lambda, h_z)\, N_i(z)\ , \tag{9}$$

where $\sigma_{ei}(\lambda, h_z)$ is obtained after interpolation of $\sigma_{ei}(\lambda, h)$ given by Eq. (6) to the humidity at altitude z, which is given in the MERRA input data file. The scattering coefficient of tracer i, $s_i(\lambda, z)$, and total scattering coefficient, $s(\lambda, z)$, are calculated similar to Eqs. (8) and (9) replacing $\sigma_{ei}(\lambda, h_z)$ by $\sigma_{si}(\lambda, h_z)$. The phase function (scattering matrix element (1,1)) for MERRA aerosol type is calculated as follows:

$$F(\lambda, z) \ = \ \frac{1}{s(\lambda, z)} \sum_{i=1}^{15} s_i(\lambda, z)\, F_i(\lambda, z)\ , \tag{10}$$

where $F_i(\lambda, z)$ is a scattering matrix element of tracer i.

In order to use MERRA aerosol type within SCIATRAN, the user needs to provide Mass-Mixing Ratio (MMR) file for a given time and geographical location. To facilitate the usage of this aerosol type for inexperienced users, MMR files for typical aerosol scenarios (e.g., dust, biomass burning, urban pollution, and

Table 5: Maximal and minimal radius of the particle size bins for dry sea salt and dust

Bin number	Dry sea salt		Dust	
	r_{min} (μm	r_{max} (μm)	r_{min} (μm)	r_{max} (μm)
1	0.03	0.1	0.1	1.0
2	0.1	0.5	1.0	1.8
3	0.5	1.5	1.8	3.0
4	1.5	2.0	3.0	6.0
5	5.0	10.0	6.0	10.0

sea salt) are included in the SCIATRAN database. Details of how to prepare the MMR file as a SCIATRAN input for specific time and geographical location can be found in the user guide and in headers of MMR files for typical aerosol scenarios.

The MERRA aerosol type is operationally used to derive NASA MERRA aerosol properties dataset. The MERRA aerosol data products are widely used in the IPCC report (Randles et al., 2017).

Implementations of other aerosol types in SCIATRAN are on-going. For instance, the use of Aerosol Robotic Network (AERONET) measurement data (e.g., RI and PSD) as direct input for the radiative transfer simulations. The users are also encouraged to send their own ideas and requests to us.

4.2. Clouds and snow

The SCIATRAN software package includes water droplets and ice crystals optical parameters database (scattering matrices, scattering and extinction cross sections), which enables to calculate radiative transfer through liquid water, ice, mix-phase clouds and snow layers. Additionally, an absorber (e.g., soot) within cloud layer (Rozanov et al., 2014) can be accounted for by adding a specific aerosol type.

4.2.1. Liquid water cloud database

The version of SCIATRAN described by (Rozanov et al., 2014) includes optical parameters (scattering matrices, extinction and scattering cross-sections) of water droplets with effective radius between 4 and 20 μm (in step of 2 μm) in the spectral range from 0.2 to 40 μm. The new implementation extends the range of the effective radius to 2 - 40 μm. The optical properties of liquid water clouds are pre-calculated using the Mie code (Mishchenko et al., 1999). The refractive index of pure water was selected according to Segelstein (1981). The water droplet size distribution was assumed to be gamma distribution:

$$f(r) \;=\; \frac{N_d\, r^{\eta}}{\Gamma(\eta+1)} \left(\frac{\eta}{r_m}\right)^{\eta+1} \exp\left(-r\frac{\eta}{r_m}\right) , \qquad (11)$$

where N_d is the number density of water droplets, r_m and η are the mode radius and half-width parameter, respectively, $\Gamma(\eta+1)$ is the gamma function. As in the previous version of SCIATRAN, the half-width parameter is set to 6. Recall that the relationship between mode radius and effective radius, r_e, is given by $r_e = r_m\,(1+3/\eta)$ (Kokhanovsky, 2006).

The SCIATRAN software offers a possibility to introduce a vertical inhomogeneity within a liquid water cloud considering N_d and r_e as functions of altitude. At the same time, the vertical coordinate, z, within a cloud is defined by employing the concept of dimensionless "altitude" as suggested by Feigelson (1981), i.e., it is introduced as $x = (h_t - z)/(h_t - h_b)$, where h_t and h_b are the top and bottom heights of the cloud layer, respectively. Thus, to introduce an inhomogeneity the user needs to specify $N_d(x)$ and $r_m(x)$ as functions of the dimensionless coordinate x, which ranges from 0 to 1.

The water droplet database within SCIATRAN software was employed, e.g., to derive the cloud optical thickness and water droplets effective radius (Mei et al., 2019) and to retrieve the vertical profile of droplets effective radius (Kokhanovsky and Rozanov, 2012).

4.2.2. Ice cloud and snow layer database

The previous ice cloud database in SCIATRAN only included optical parameters of two ice crystal shapes, namely fractal of second generation (Macke et al., 1996) and hexagonal prism. Moreover, the optical characteristics were pre-calculated within a limited range of ice crystal size. In particular, for second generation fractal the tetrahedron side length was set to 50, 100 and 300 μm, which corresponds to the effective radius of 23, 46 and 142 μm, respectively. For hexagonal prism, the optical properties were pre-calculated for hexagonal prism height of 100 μm and side lengths of 12.5, 25 and 50 μm.

The limited range of ice crystal sizes can introduce large uncertainties in the ice cloud effective radius retrieval (Mei et al., 2018a). To overcome this problem, ice crystal databases developed by Baum et al. (2011) and Yang et al. (2013) were also included in the SCIATRAN software. These ice cloud databases were operationally used to derive NASA cloud properties dataset from MODIS (King et al., 2013, Platnick et al., 2017).

The Baum ice crystal database contains optical parameters of "AggregateSolidColumns" shape of ice crystals in the spectral range 0.2 - 99 μm with effective radius between 5 and 60 μm, and the step of 2.5 μm.

The Yang database contains optical parameters of eleven ice crystal shapes, following Pohl et al. (2020), nine shapes are included in SCIATRAN software, i.e., aggregate of 8 columns, droxtal, hollow bullet rosettes, hollow column, plate, aggregate of 5 plates, aggregate of 10 plates, solid bullet rosettes, and column. The optical parameters include extinction efficiency, extinction cross-section, single scattering albedo and six elements of the scattering matrix pre-calculated for maximal dimension of ice habits between 2 and 10000 μm in the spectral range from 0.2 to 15.25 μm. The extinction cross-section, single scattering albedo, non-zero elements of scattering matrix, effective radius, projected area, and volume of each habit at 189 dimensions were used from original Yang database. The expansion coefficients were calculated expanding the elements of scattering matrix in the generalised spherical functions. Additional details and

some applications can be found in Pohl et al. (2020).

It is worth noticing that for the same maximal dimension of ice crystal, its effective radius depends on its shape. For instance, the maximal dimension of $700\,\mu$m results in effective radius of $295.3\,\mu$m for a droxtal while it is $53.0\,\mu$m for a plate. The relationship between maximal dimension and effective radius for crystals of different shape is reported by Yang et al. (2013) and also included in the SCIATRAN database.

Natural ice cloud layers are usually composed of polydisperse ice crystals of different shapes (Baum et al., 2005). For Yang database, the polydispersity and habit mixture, can be considered in SCIATRAN using PSD function and a desired habit ratio, respectively. In particular, to describe polydisperse properties of habit mixture, the gamma distribution with respect to the maximal dimension, D, following Saito et al. (2019), is used:

$$n(D) = N_c\, C\, (D/D_0)^{k-1}\, \mathrm{e}^{-(k-1)\, D/D_0}\ . \tag{12}$$

Here, N_c is the number of ice crystals per unit volume, k and D_0 are the shape and mode parameter, C is the normalization factor. The number density, N_c, and mode, D_0, can be selected as constant within ice cloud layer or depending on the altitude. This enables users to formulate a realistic model of a vertically inhomogeneous, polydisperse crystal habit mixture of an ice cloud and snow layer.

Similar to the snow grain habit mixture model used by Saito et al. (2019), the habit mixture implemented into SCIATRAN depends on the dimension of ice crystals. In particular, user can pre-define mixing ratios $f_h(D_i)$ of any aforementioned ice particle habit, h, at specific dimension grid point D_iṠCIATRAN interpolates the mixing ratios linearly (other interpolation type is not available) with respect to $\ln D$ between division points (as recommended in Saito et al. (2019)) and calculates the bulk optical properties of ice particle habit mixture by weighting the single-habit properties according to their mixing ratio. Following Baum et al. (2011), the scattering and extinction cross-sections as well

as the scattering matrix are calculated as:

$$\sigma_p = \sum_{h=1}^{N_h} \int_{D_1}^{D_2} f_h(D)\, \sigma_{p,h}(D)\, n(D)\, dD \,, \tag{13}$$

$$\mathbf{F}(\gamma) = \frac{1}{\sigma_s} \sum_{h=1}^{N_h} \int_{D_1}^{D_2} f_h(D)\, \mathbf{F}_h(\gamma, D) \sigma_{s,h}(D)\, n(D)\, dD \,, \tag{14}$$

where N_h is the number of habits, the subscript p denotes 's' or 'e' for the scattering, $\sigma_{s,h}(D)$, or extinction, $\sigma_{e,h}(D)$, cross-section, respectively, $\mathbf{F}_h(\gamma, D)$ is the scattering matrix of habit h having dimension D, and

$$\sum_{h=1}^{N_h} f_h(D) \;=\; 1 \,. \tag{15}$$

The integrals in Eqs. (13) and (14) are calculated by SCIATRAN numerically using trapezoidal rule and partition of the interval $[D_1 = 2\,\mu m, D_2 = 10000\,\mu m]$ is performed according to the discrete grid used by Yang et al. (2013). In particular, the intervals are 1, 2.5, 12.5, 125 μm for the ranges [2 - 10], [10 - 100], [100 - 1000], [1000 - 10000] μm, respectively.

As mentioned above, the SCIATRAN software enables the user to introduce a vertical inhomogeneity within an ice cloud or snow layer considering N_c and D_0 as functions of depth. In this case the approach of dimensionless "altitude" is employed as described above for a liquid water cloud. Thus, the user needs to specify $N_c(z)$ and $D_0(z)$ as functions of the dimensionless coordinate x, which ranges from 0 to 1.

For a vertically homogeneous mono-disperse habit-mixture cloud, the input parameters include the optical thickness of the cloud, maximal dimension and fractions of the selected ice crystal shapes. Combining the liquid water and ice crystals optical properties, the radiative transfer calculations can also be performed for a mix-phase cloud.

The database of the optical properties of ice crystals proposed by Yang et al. (2013) was successfully utilized to 1) estimate impact of habit mixture on the simulated Top Of the Atmosphere (TOA) reflectance from Polarization and directionality of Earth reflectances (POLDER) instrument (Pohl et al., 2020);

2) derive snow properties research products (snow grain size and shape) using TOA reflectance measurements from Copernicus Sentinel-3 Sea and Land Surface Temperature radiometer (SLSTR) instrument in the framework of the XBAER algorithm (Mei et al., 2021a,b).

Although it has been demonstrated that the database of the optical properties of ice crystals proposed by Yang et al. (2013) can be used for snow studies, a realistic model of a snow layer is usually represented by a vertically inhomogeneous, polydisperse ice crystal habit mixture (Mei et al., 2021a), which requires a-priori knowledge of several properties of the snow layer (e.g., appropriate numbers of habits and their fraction as well as parameters of PSD function).

To simplify the requirements for such a-priori knowledge, we have also implemented in the SCIATRAN software a stochastic mixture model of ice crystals and air gaps based on the stereological approach (Malinka, 2014). In the framework of the stereological approach (geometrical statistic) the snow layer is considered as two-phase random mixture of ice particles and air gaps. The grains of irregular shapes are characterized in that case by random chord length distribution. Under random chord we understand a straight line connecting any two points on the border inside the ice crystal or air gap. The chord length is a random value, which is determined by some distribution function. With an assumption of a stochastic ice crystal mixture, this approach uses the concept of the chord length distribution rather than the characteristics of a separate crystal. The theoretical background to calculate optical parameters of corresponding stochastic snow model can be found in (Malinka, 2014, 2015).

The usage of stochastic model has at least two advantages as compared to Yang et al. (2013) database. First, the stochastic model does not require any database because the optical parameters can be easily calculated online. Second, for a vertically homogeneous snow layer, users only need to have information about mean chord of ice crystals and the optical thickness of the snow. The mean chord length plays the role of the effective size of a ice crystal, namely mean chord coincides with the factor of 3/4 with the standard definition of the effective radius (Malinka, 2014).

Table 6: Mean chords and optical thicknesses of different surface types (Malinka et al., 2016)

Surface type	Mean chord (μm)	Optical thickness
Bright white ice	450 - 720	14 - 50
Typical white ice	2200 - 2800	9 - 20
Melting ice	4700 - 10000	2.2 - 5.4
Snow-covered ice	170 - 270	27 - 73

We recall, however, that the usage of stochastic model is reasonable if the size of ice particles is significantly larger than the wavelength. Retrieved values of mean chords and optical thicknesses of different white ice types according to Malinka et al. (2016) are summarized in Table 6.

4.3. Surface reflection

Surface albedo or BRDF are important parameters in RT calculations. The SCIATRAN software includes both Lambertian albedo and various BRDF models (Rozanov et al., 2014). In the case of Lambertian reflection, user can select spectral dependent or constant albedo. In particular, global dataset of vegetation and land albedo (Matthews, 1983) is available in the SCIATRAN software. For RT calculations accounting for a surface BRDF, users can choose one of the following built-in models: RPV (Rahman et al., 1993), kernel-based Ross-Li (also called RTLSR) (Maignan et al., 2004, Roujean et al., 1992), kernel-based Ross-Li vegetation-soil (Breon and Vermote, 2012), modified RPV plus facet (Diner et al., 2012). A brief description of aforementioned models is given in Appendix B.

For a retrieval of surface properties from satellite observations, the following surface reflectance models are additionally included in SCIATRAN software: PROSAIL, XBAER, snow and melt ponds on sea ice.

In order to facilitate users to select a proper BRDF model, following general recommendations can be formulated.

- The multi-parameter PROSAIL model is recommended to investigate the sensitivity of surface and TOA reflectances with respect to the biophysical vegetation parameters on a local or regional scale.
- The single-parameter XBAER model can be advised for investigations of surface and TOA reflectances on a global scale because only one parameter is needed for this model.
- The RPV and RTLSR models are recommended for modeling of multi-angle scalar observations of BRDF in case of a snow-free land surface.
- The modified RPV plus facet model is suitable for modeling multi-angle polarized observations of BRDF in case of a snow-free land surface.
- The FASMAR and RTLSRS models are recommended for simulations of multi-angle scalar observations of BRDF for snow covered surfaces.

4.3.1. PROSAIL model for vegetated surfaces

The PROSAIL model is a combination of the PROSPECT and SAIL (Scattering by Arbitrary Inclined Leaves) models (Jacquemound et al., 2009). The PROSAIL is used to describe the directional reflectance of plant canopy and retrieve biophysical properties of vegetation.

The PROSAIL source code (http://osr-cesbio-ups-tlse.fr) was adopted and implemented into the SCIATRAN software. The input parameters are leaf inclination distribution function type, Leaf Area Index (LAI), hot spot parameter, chlorophyll content, carotenoid content, brown pigment content, Equivalent Water Thickness (EWT), Leaf Mass per Area (LMA), structure coefficient and soil factor.

Using a desired model of the atmosphere in combination with BRDF provided by the implemented PROSAIL model, user can calculate the radiation field in the atmosphere in UV, VIS, and NIR spectral ranges accounting for the angular scattering properties of a vegetated surface. To verify the implementation of the PROSAIL model, a comparison of TOA reflectances simulated by SCIATRAN

and measured by the MODIS instrument is presented in Sect. 6 (see upper panel of Fig. 4).

4.3.2. XBAER land surface reflectance parameterization

The XBAER model describes the surface reflectance by a linear relationship with respect to Soil Adjusted Vegetation Index (SAVI) (Mei et al., 2017a). This model was originally designed for the AOT retrieval in the framework of the XBAER algorithm (Mei et al., 2017a) using measurements of the MERIS instrument. For wavelengths above the red-edge (MERIS channels 10, 12, 13 and 14, which correspond to 753, 778, 865 and 885 nm), the surface reflectance, $R(\lambda_i)$, was approximated as

$$R(\lambda_i) \;=\; a(\lambda_i)\, x + b(\lambda_i), \quad i = 10, 12, 13, 14, \tag{16}$$

where i is the MERIS channel number, $a(\lambda_i)$ and $b(\lambda_i)$ are the slope and intercept for given wavelengths λ_i in the Surface Reflectance Wavelength Shape Constrain Database (SRWSCD) (Mei et al., 2017a) and x is SAVI.

For wavelengths below the red-edge (MERIS channels 1,2,...,9, which correspond to 412, 443, 490, 510, 560, 620, 665, 681 and 708 nm), the ratio between the surface reflectance at each wavelength, λ_i, and the surface reflectance at the MERIS channel 14 was parameterized by

$$R(\lambda_i)/R(\lambda_{14}) \;=\; \tilde{a}(\lambda_i)\, x \;+\; \tilde{b}(\lambda_i), \quad i = 1, 2, ..., 9. \tag{17}$$

The SRWSCD database, which belongs to the XBAER retrieval algorithm and is not included in the SCIATRAN database, includes the geographic dependent monthly slope and intercept of the linear model.

Regression coefficients for typical surface types (e.g., vegetated surface, urban, desert) are included in the SCIATRAN database. Using the data files for these typical surface types as templates, users can prepare their own regression coefficients following Mei et al. (2017a).

A comparison of simulated TOA reflectances obtained utilizing XBAER parameterization and PROSAIL model are presented in Sect. 6 (see upper panel of Fig. 4).

4.3.3. Snow and melt ponds on sea ice

Besides the modified RPV (Degunther and Meerkotter, 2000) and asymptotic model (Kokhanovsky and Zege, 2004) of the snow reflectance, the recent snow kernel-based BRDF models, such as RTLSRS and FASMAR suggested by Jiao et al. (2019) and Mei et al. (2022), respectively, as well as the model of white ice and melt ponds on sea ice (Malinka et al., 2016, 2018) were also included.

RTLSRS model.

The kernel-driven RossThick-LiSparseReciprocal BRDF model with snow kernel (RTLSRS) (Jiao et al., 2019) was implemented in the following form:

$$\rho(\Omega,\lambda) \;=\; f_i(\lambda) + f_v(\lambda)K_v(\Omega) + f_g(\lambda)K_g(\Omega) + f_s(\lambda)K_s(\Omega)\;, \qquad (18)$$

where f_i, f_v, f_g, and f_s are wavelength-dependent coefficients, Ω comprises angular variables $\{\vartheta_0, \vartheta, \varphi\}$, which describe solar zenith angle, viewing zenith angle and relative azimuth, respectively, λ is wavelength, K_v, K_g, and K_s are the volumetric scattering kernel, geometric-optical kernel and snow kernel, respectively.

As compared to the classical Ross-Li model suggested by Lucht et al. (2000), an additional snow kernel based on the asymptotic model of Kokhanovsky and Zege (2004) was introduced to describe the strong forward scattering peak typical for the snow reflection. Although the SCIATRAN software does not contain a database of the coefficients $f_i(\lambda)$, $f_v(\lambda)$, $f_g(\lambda)$, and $f_s(\lambda)$, the kernels are included. The user needs to provide a file containing the coefficients at a discrete number of wavelengths. Some examples of the coefficients obtained by fitting the RTLSRS model to the measured TOA reflectance are presented in Jiao et al. (2019). The file structure is described in the user guide.

FASMAR.

In contrast to the RTLSRS model, where the snow kernel based on the ART model (Kokhanovsky and Zege, 2004) was used to improve the accuracy in the case of a snow reflection, FASMAR exploits the ART model as a main kernel. In particular, FASMAR (see (Mei et al., 2022) for details) includes 4 kernels and the model is formulated as

$$\rho(\Omega,\lambda) \;=\; f_1 + f_2\,K_2(\Omega,\lambda) + f_3\,K_3(\Omega,\lambda) + f_4\,K_4(\Omega) + f_5\,K_5(\Omega)\;, \qquad (19)$$

where $f_1, f_2, \ldots, f_5$ are wavelength dependent parameters (argument λ is omitted), and the kernels are given by

$$K_2(\Omega,\lambda) \;=\; R^0_\infty(\Omega)\,\mathrm{e}^{-\beta_\lambda\,A(\Omega)} \;-\; k_2(\lambda)\;, \qquad (20)$$

$$K_3(\Omega,\lambda) \;=\; p_\lambda(\theta)/(\mu+\mu_0)/4 \;-\; k_3(\lambda)\;, \qquad (21)$$

$$K_4(\Omega) \;=\; R^0_\infty(\Omega)\,\mathrm{e}^{\cos\theta} \;-\; k_4\;, \qquad (22)$$

$$K_5(\Omega) \;=\; \cos\theta \;-\; k_5\;. \qquad (23)$$

In the right hand side of each equation the second term is introduced which modifies the respective kernel to obtain $K_2 = K_3 = K_4 = K_5 = 0$ for SZA=0° and VZA=0°. The modification terms are given by

$$k_2(\lambda) = R^0_\infty(\tilde\Omega)\,\mathrm{e}^{-\beta_\lambda\,A(\tilde\Omega)}\;,\; k_3(\lambda) = \frac{p_\lambda(-1)}{8}\;,\; k_4 = \frac{R^0_\infty(\tilde\Omega)}{2.718}\;,\; k_5 = -1\;. \qquad (24)$$

As a result, the coefficient f_1 gives the magnitude of the reflectance in the nadir direction (Roujean et al., 1992). In Eqs. (20) - (24), $\mu = \cos\vartheta$, $\mu_0 = \cos\vartheta_0$, ϑ_0, ϑ and θ are solar zenith angle, viewing zenith angle and scattering angle, respectively, $\tilde\Omega = \{0,0,0\}$, $\beta_\lambda = \sqrt{\gamma_\lambda\,d}$, $\gamma_\lambda = 4\pi\,\kappa_i/\lambda$ is the absorption coefficient of ice, κ_i is the imaginary part of the ice refractive index, d is an effective grain size, defined by the ratio of the average volume to the average surface area of grains, $p_\lambda(\theta)$ is the phase function, and $R^0_\infty(\Omega)$ is the reflection function of semi-infinite non-absorbing media.

FASMAR includes the ART kernel, K_2, a single-scattering kernel, K_3, and auxiliary kernels, K_4 and K_5. The kernel K_5 is only used for wavelengths longer than 1600 nm. In kernel K_2, the function $R^0_\infty(\Omega)$ is implemented according to the

approximation suggested by Kokhanovsky (2005), the function $A(\Omega)$ is given by $A(\Omega) = b_n\, K_0(\mu)\, K_0(\mu_0)/R^0_\infty(\Omega)$ (Kokhanovsky and Zege, 2004), where $K_0(\mu)$ is called the escape function, which is implemented according to the common approximation (Sobolev, 1972) as $K_0(\mu) = 3/7(1 + 2\mu)$. The parameter b_n depends mainly on the ice crystal shape. For the fractal ice particles, it was estimated by Kokhanovsky and Zege (2004) to be 3.62. As a result, the final expression for $A(\Omega)$ is given by $A(\Omega) = 0.66\,(1 + 2\mu)(1 + 2\mu_0)/R^0_\infty(\Omega)$.

Similar to the RTLSRS model, the SCIATRAN software does not contain database of the coefficients $f_1, f_2, \ldots, f_5$. The user needs to provide a file containing the coefficients at a discrete number of wavelengths. The file structure is described in the user guide.

Comprehensive comparisons of FASMAR and RTLSRS models with ground-based, aircraft and satellite measurements of snow angular reflectance can be found in Mei et al. (2022). FASMAR can be used for large solar zenith angles (e.g., SZA $> 80°$, which is a typical case the polar regions) while both Ross-Li and the RTLSRS models are recommended to be used for SZAs $< 70°$.

White ice and snow-covered ice reflectance model.

White ice and snow-covered ice are two typical surface types in the polar regions. Following Malinka et al. (2016), the white ice BRDF model describes reflection an ice layer with a highly scattering granular layer on top. Since the grain size of ice crystals is significantly larger than the wavelength of incident light, the optical parameters (extinction coefficient, SSA, and phase function) of a stochastic mixture of irregular ice crystals and air gaps were analytically derived by Malinka (2014, 2015). Using the analytical expressions for optical parameters and employing asymptotic radiative transfer theory, the following analytical expression for BRDF of white ice was proposed by Malinka et al. (2016) and implemented into SCIATRAN:

$$R = R^0_\infty \frac{\sinh\left\{\gamma\,\tau + y\,[1 - K(\vartheta)K(\vartheta_0)/R^0_\infty]\right\}}{\sinh(\gamma\,\tau + y)}\,, \tag{25}$$

where R^0_∞ is the BRDF of a non-absorbing semi-infinite layer with the same scattering phase function as the snow layer, sinh denotes the sinus hyperbolicus,

τ is optical thickness of the snow layer, ϑ_0 and ϑ are incidence and observation polar angles, respectively,

$$\gamma = \sqrt{3\,(1-\omega)\,(1-\omega\,g)}\;, \qquad K(\vartheta) = \frac{3}{7}\,(1+2\,\cos\vartheta)\;, \tag{26}$$

$$y = 4\,\sqrt{\frac{(1-\omega)}{3\,(1-\omega\,g)}}\;, \qquad K(\vartheta_0) = \frac{3}{7}\,(1+2\,\cos\vartheta_0)\;. \tag{27}$$

The expression for the single scattering albedo is

$$\omega = 1 - \frac{\alpha\,n^2\,a\,T_{dif}}{\alpha\,n^2\,a + T_{dif}}\;, \qquad \alpha = \frac{4\,\pi\,\kappa}{\lambda} + \alpha_y\;, \tag{28}$$

where n and κ are the real and imaginary parts of the ice refractive index, a is mean chord of ice crystals and α_y is the absorption by the yellow substance in the white ice. Analytical expressions for asymmetry factor (g), α_y, and auxiliary function T_{dif} are given in Appendix C.

The usage of Eq. (25) to calculate BRDF in the framework of SCIATRAN software requires the following parameters to be provided by the user: optical thickness of the snow layer, τ, mean chord of ice crystals, a, and yellow substance absorption coefficient, α_y. The refractive index of ice can be either taken from the SCIATRAN database or provided by the user. The calculation of R^0_∞ is performed by SCIATRAN using a pre-calculated look-up-table.

Melt ponds on sea ice reflectance model.

The BRDF model of melt ponds on sea ice (Malinka et al., 2018) was implemented into SCIATRAN as follows:

$$R_\lambda(\Omega) = \frac{1}{\mu_0}\,R_F(\mu_0)\,\delta(\mu-\mu_0)\,\delta(\varphi) + \frac{T_F(\mu)\,T_F(\mu_0)\,A_b}{\pi n^2[1-A_b\,f_{in}(\tau_p)]}\,e^{-\tau_p/\mu_0'-\tau_p/\mu'}\;. \tag{29}$$

Here, $R_F(\mu_0)$ and $T_F(\mu_0)$ are the Fresnel reflectance and transmittance of a flat water surface for the cosine of the incidence angle μ_0, n is the refractive index of water (assuming refractive index of air to be 1), μ_0' is the cosine of the refractive angle ($\sqrt{1-\mu_0^2} = n\,\sqrt{1-\mu_0'^2}$) , $\tau_p = z\,\sigma_p$ is the optical thickness of pond, z is the pond depth and σ_p is the extinction coefficient of the water, equal to the sum of the water absorption (α_w) and scattering (σ_w) coefficients, $\delta(\mu-\mu_0)$ and $\delta(\varphi)$ are the Dirac delta functions (Korn and Korn, 1968). A_b is

the pond bottom albedo. The auxiliary function $f_{in}(\tau_p)$ (Malinka et al., 2018) is calculated numerically by the SCIATRAN program. For simplicity reasons, the dependence of R_F, T_F, A_b, n, and τ_p on the wavelength, λ, is not indicated. The analytical expression for albedo of an under-pond ice layer, A_b, as a function of the geometric thickness of the under-pond ice, H, and transport scattering coefficient, σ_t, is given in Appendix D.

To calculate BRDF using Eq. (29) in the framework of the SCIATRAN software the following input parameters need to be provided by the user: geometric thickness of the under-pond ice, H, water layer (pond) depth, z, and transport scattering coefficient, σ_t. Following Malinka et al. (2018), the reasonable range for σ_t is [0.2 - 10] m^{-1}. In particular, for light and dark melt ponds, typical values for σ_t are ~ 4 and $\sim 2\,\mathrm{m}^{-1}$, respectively. Water absorption and scattering coefficients as well as refractive indices of water and ice can be either taken from SCIATRAN databases or provided by the user.

5. Inherent optical properties of aerosol and clouds

5.1. Aerosol

Fig. 2 shows an example of the optical properties of the aerosol types newly implemented in SCIATRAN. All optical properties are calculated using AOT of 0.5 at the wavelength of 0.55 μm. For MODIS-DT, moderately absorbing aerosol type is selected. For MODIS-OC, two basic components F1 and C2, see Table 3, are selected and the fine mode fraction is set to 0.5. For XBAER-OC, purely maritime aerosol type is selected. For Dubovik dust model, the aspect ratio is set to 1. For OPAC 4.0 dust model, the total number of mineral particles is set to 300 representing the "background desert conditions" (Köpke et al., 2015). In the "background desert conditions", the fractions of mineral nuceation model, mineral acumulation mode and mineral coarse model are 89.79%, 10.16%,0.05%, respectively. In this paper, the same components and fractions were used for

OPAC 3.0 dust model. The MERRA aerosol type is selected for the AERONET site Rio-Branco (-67.869°E, -9.957°N) on 16 August, 2020. With the above settings, the MODIS-DT and MERRA (picked up at the same time and location), MODIS-OC and XBAER-OC (both represent the maritime aerosol type), Dubovik dust , OPAC 3.0 and OPAC 4.0 dust (both represent the dust aerosol type) are sub-groups within which optical properties are expected to be comparable.

In Fig. 2(a), the wavelength dependent AOTs calculated using different aerosol types show the same value at 550 nm because all optical properties are scaled to AOT = 0.5 at this wavelength. The Angstrom coefficients (in the spectral range 440 - 870 nm) are 1.77 and 1.81 for MODIS-DT and MERRA, -0.19 and -0.11 for MODIS-OC and XBAER-OC, 0.56,-0.009 and 0.01 for Dubovik dust, OPAC 3.0 and OPAC 4.0 dust, respectively. The lines of the MODIS-DT and MERRA aerosol types almost overlap, indicating the similarity of aerosol properties. MODIS-OC and XBAER-OC show a similar spectral pattern with AOT slightly increasing with the wavelength. This can be explained by the significant contribution of coarse mode particles. The Dubovik dust shows a much stronger spectral gradient as compared to OPAC 4.0 dust.

Fig. 2(b) shows the phase functions at 550 nm for the selected aerosol types. In the case of MERRA, the phase function is selected for an altitude near the surface. As expected, MODIS-DT and MERRA, MODIS-OC and XBAER-OC, Dubovik, OPAC 3.0 and OPAC 4.0 dust have similar phase functions, respectively. Coarse-mode dominated aerosol types (MODIS-OC, XBAER-OC, Dubovik and OPAC 4.0) show stronger forward peak scattering as compared to fine-mode dominated aerosol types (MODIS-DT and MERRA). For the selected scenario, MODIS-DT shows a stronger forward scattering and a weaker backward scattering as compared to MERRA. MODIS-OC and XBAER-OC, with completely different parameterization strategies, show very similar phase functions. OPAC 3.0 and OPAC 4.0 show similar behavior while Dubovik and OPAC 4.0 dust models show relatively large difference both in the forward and backward scattering as compared to other aerosol types (e.g., MODIS-DT and

MERRA, XBAER-OC and MODIS-OC).

Fig. 2(c) shows the wavelength-dependent Single Scattering Albedo (SSA) for the selected aerosol types. MODIS-DT and MERRA show large difference in the absolute SSA values, however, both demonstrate the increase of absorption with the wavelength. MODIS-OC and XBAER-OC, especially XBAER-OC, demonstrate weak absorption. The Dubovik and OPAC 4.0 dust models show again differences in both magnitude and wavelength dependence.

Fig. 2(d) shows the wavelength dependent asymmetry factor, g, for the selected aerosol types, which is a fundamental property of aerosol particle that affects the aerosol direct radiative forcing. MODIS-OC and XBAER-OC show the largest g values indicating a stronger forward scattering while MODIS-DT and MERRA show the smallest g indicating a weaker forward scattering, which is consistent with the results presented in Fig. 2(b).

5.2. Cloud

A comprehensive consideration of the extinction efficiency, single-scattering albedo, and asymmetry factor for different wavelengths, maximum dimensions, and selected crystal shapes can be found in (Yang et al., 2013). In the scope of this paper we consider only the phase functions of ice crystals in the visible spectral range, where, owing to weak absorption by ice and water, the scattering processes play a very important role.

Fig. 3 shows the comparison of water droplets and ice crystals phase functions with campaign measurements provided by Jarvinen et al. (2018). The phase functions are presented at the wavelength of 532 nm and normalized to the Arctic CLoud Observations Using airborne measurements during polar Day (ACLOUD) measurement at a scattering angle of 18 ° (Jarvinen et al., 2018). The effective radii of water droplets and ice crystals are selected to be the global mean values of about 13.5 μm and 25 μm, respectively (King et al., 2013).

As expected, the phase function of water droplets is quite different from those

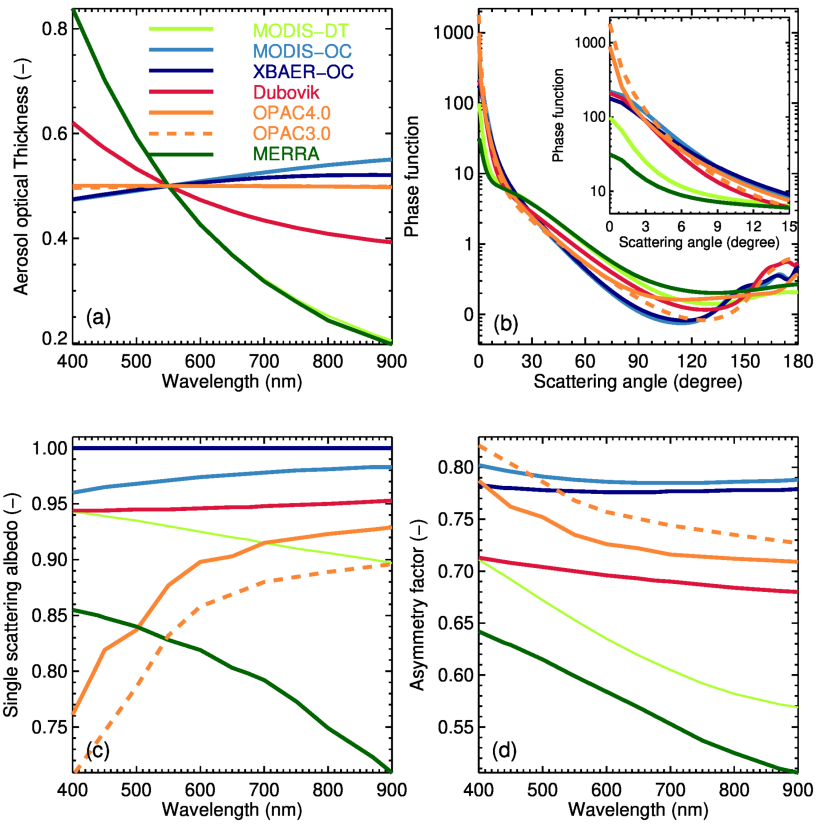

Figure 2: Optical properties of the aerosol types newly implemented in SCIATRAN (indicated by different colors): (a) wavelength dependent AOT; (b) phase function at a wavelength of 0.55 μm (with a zoom-in panel in the upper right corner); (c) wavelength dependent single scattering albedo; (d) wavelength dependent asymmetry factor.

of ice crystals, especially at backward scattering directions. In particular, the famous rainbow feature of the scattering by water droplets can be observed at about 138°. The large differences in the phase functions observed by different campaigns indicates the large variability of cloud optics. Large differences are observed mainly in the backward scattering direction. For ice crystals, aggregate of 8 columns and droxtal have the strongest backward scattering while plate shows the weakest one. The large variability of the campaign measurements can be well described by a mixture of different ice crystal shapes.

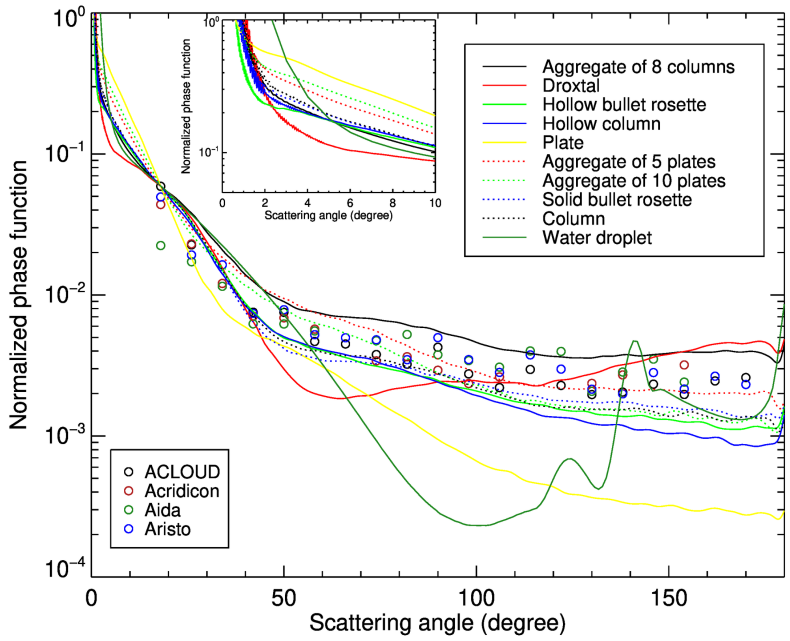

Figure 3: Comparison of phase functions for water droplets and ice crystals with campaign measurements provided by Jarvinen et al. (2018). Symbols - measurements, lines - different shapes (see legend). A zoom-in panel for smaller scattering angles is shown in the upper left corner of the plot.

6. Simulated TOA reflectance for different CAS scenarios

In this section we consider selected applications of aerosol and cloud databases and BRDF models for calculations of TOA reflectance for a surface-atmosphere system using SCIATRAN software. The following surface scenarios are considered below: snow, white ice and melt ponds typical for high latitude regions and vegetated surface typical for low and middle latitude regions.

Vegetated surface

Simulations presented in this sub-section are performed using the veiwing geometry and the spectral response function of the HyperSpectral Imager (HSI) instrument onboard the Environmental Mapping and Analysis Program (EnMAP) mission. HSI/EnMAP is a German perspective mission to monitor environment-related parameters launched in April 2022 and XBAER is a candidate algorithm to provide CAS products for this instrument.

Example simulations of the TOA reflectance with SCIATRAN for different scenarios were performed for the AERONET site Rio-Branco (-67.869°, -9.957°) in the Amazon region for 16 August, 2020. The surface reflectance was calculated by using either the XBAER parameterization or the PROSAIL model. The SAVI parameter required by the XBAER parameterization was estimated from measurements of the Ocean and Land Colour Instrument (OLCI) as 0.34. Due to database limitations the simulations using XBAER parameterization were done only for OLCI wavelengths. The PROSAIL model was used with LAI of 4.5, which was obtained from the MODIS LAI product. Leaf inclination distribution function type was set to Type = 1 (Spherical). Other parameters are set as follows: hot spot parameter (0.01); chlorophyll content ($1\,\mu g/cm^2$); carotenoid content ($8\,\mu g/cm^2$); brown pigment content (0); EWT (0.01 cm); LMA ($0.009\,g/cm^2$); structure coefficient (1.5); soil factor (1.0).

The aerosol was accounted for by using the MERRA aerosol type with fraction of each component provided by MERRA data base for the selected time and location. In particular, AOTs of the total column, Black Carbon, Organic

Carbon, Sulfate, Sea Salt, and Dust are 0.241, 0.043, 0.143, 0.043, 0.003, and 0.009, respectively. A water cloud between 2.0 and 2.5 km with Cloud Optical Thickness (COT) of 3 and effective radius of water droplets of 13.5 μm was used for simulations. Along with aerosol, cloud, and Rayleigh scattering the absorption by all relevant atmospheric gases was accounted for. The vertical profiles of pressure, temperature, and absorber number density were taken from the database created with the Bremen 2D Chemical Transport Model (Sinnhuber et al., 2009) for August at the latitude of 10°S.

TOA reflectances simulated with SCIATRAN for different scenarios are shown in the upper panel of Fig. 4. For comparison, TOA reflectances measured by the MODIS instrument at the same time and location are also presented. One can see that for clear sky scenarios (S+R+A and S+R+A+G) the TOA reflectances simulated using both XBAER surface parameterization and PROSAIL model agree well with reflectances observed by MODIS. The red-edge effect and sharp spectral structures are from vegetation and gas absorption, respectively. The plot indicates that employing the newly implemented features in the SCIATRAN model, the wavelength dependence and the magnitude of TOA reflectance observed by MODIS can be well reproduced by the simulations.

For the cloudy scenario (S+R+A+G+C) one observes a general enhancement of the TOA reflectance caused by the additional reflectance of the cloud layer. However, the contribution of surface is still visible (red edge from vegetation) because the cloud is optically thin (COT = 3).

The MERRA aerosol model used for the simulations enables us to investigate contributions of different aerosol components to the TOA reflectance. For this purpose the TOA reflectance was calculated first accounting for the contributions from all aerosol components (total) and then for each particular aerosol component independently. The calculated reflectances are shown in the lower panel of Fig. 4. In the case under consideration (over the Amazon forest), contributions of aerosol components differ for different wavelengths with the strongest contribution from organic carbon component below about 800 nm.

Snow surface

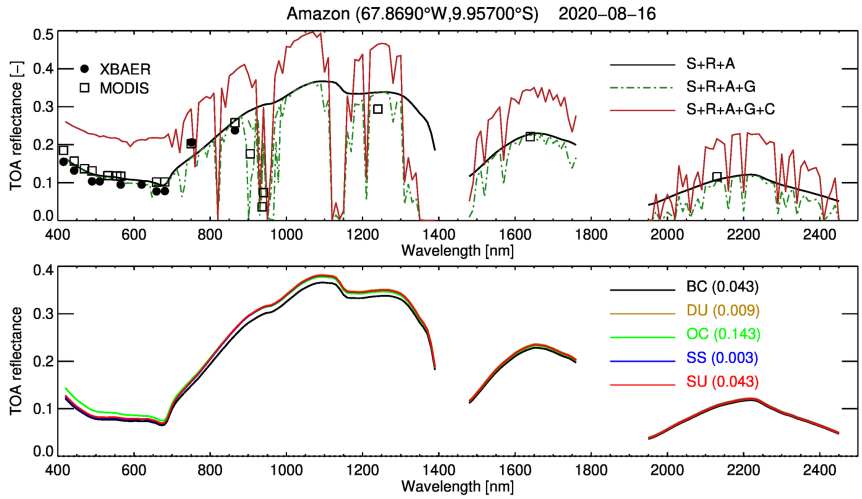

Figure 4: TOA reflectance simulation for a measurement from the EnMAP instrument over the Amazon region on 16 August, 2020. Upper panel: TOA reflectance simulated using different settings: S - surface reflectance described by the PROSAIL model, R - Rayleigh, A - Aerosol, G - Gaseous absorbers, C - Cloud. Open rectangles depict MODIS observation data and filled circles represent simulations with XBAER for OLCI wavelengths. Lower panel: TOA reflectance simulated considering different MERRA aerosol components: BC - Black Carbon, DU - Dust, OC - Organic Carbon, SS - Sea Salt, SU - Sulfate. The AOT for each component is indicated in the brackets.

This sub-section presents example results of simulations of snow reflectance performed with the radiative transfer package SCIATRAN. The snow layer was defined as a layer with an optical thickness of 5000 and a geometrical thickness of 1 m covering a black surface. The snow layer was assumed to be vertically and horizontally homogeneous without any surface roughness and composed of monodisperse ice crystals. The impact of snow impurities and scattering/absorption processes in the atmosphere was neglected. The optical properties for the droxtal ice crystal shape with effective radius of 126 μm (Mei et al., 2021b) from Yang et al. (2013) database were used for simulations.

The solar zenith angle was set to 68.9°, which corresponds to the mean value during summer at Svalbard (Mei et al., 2022).

The BRDF of the snow layer calculated with SCIATRAN is shown in the form of polar plots in the left column of Fig. 5 for wavelengths of 380, 480, 670, 870, 1220, and 2200 nm. These wavelengths are selected to represent typical spectral channels of satellite instruments (e.g., MODIS, MERIS/OLCI, AATSR/SLSTR) from UV to SWIR. For a comparison, the snow BRDF was calculated using FASMAR and RTLSRS models. The coefficients required by these models were obtained by fitting their results to SCIATRAN simulations. The relative differences of the results from FASMAR and RTLSRS models to those from SCIATRAN are presented in the middle and right columns of Fig. 5. One can see that reflectances obtained with FASMAR and RTLSRS models show very good agreement (both spectral and angular) with the SCIATRAN simulations. However, the RTLSRS model show lower reflectances in the forward direction (RAA = 0) as compared to the results from FASMAR and SCIATRAN. The relative difference between FASMAR and SCIATRAN results is within 5 % for typical satellite observation angles. A decrease of BRDF values with increasing wavelength is seen in all three datasets. This feature is caused by the ice crystal absorption.

Further examples of FASMAR and RTLSRS model comparisons with ground-based, aircraft and satellite measurements of snow angular reflectance can be found in Mei et al. (2022).

White ice and snow covered ice

Sea ice is one of the most important surface types in the high latitude ocean regions. Measurements of spectral albedo for typical sea ice conditions were performed in the spectral range 350 - 1350 nm during the R/V Polarstern cruise ARK-XXVII/3 from 2 August to 8 October 2012 (Malinka et al., 2016). Two examples of bright white ice spectral albedo measurements, as presented in Malinka et al. (2016) (see their Fig. 8(a) and (c)), are used in this paper as well. The scattering layer for these two examples is about $3-8\,\mathrm{cm}$ thick while the near surface air temperature is about -1.2 ° C. Such sea ice scenarios represent intermediate phase between a typical snow and white ice (Malinka et al., 2016). Simulations with SCIATRAN were performed using the stochastic model of the surface reflection described in Sect. 4.3.3 and an aerosol-free atmosphere without gaseous absorption. Figures 6(a) and 6(b) show comparisons of measured and modelled bright white ice spectral albedo with and without yellow substance absorption, respectively.

Three parameters required to initialise the BRDF model in SCIATRAN (snow layer optical thickness, mean chord and yellow substance absorption) were obtained by fitting the simulated albedo with respect to the measured one within the spectral range $350-1350\,\mathrm{nm}$. The following parameters provide the minimal residual between the measured and simulated spectral albedo presented in Fig. 6(a) and Fig. 6(b): ($\tau = 350.0$, $a = 510.6\,\mu\mathrm{m}$, $\alpha_y = 0.71\,\mathrm{m}^{-1}$) and ($\tau = 14.1$, $a = 776.2\,\mu\mathrm{m}$, $\alpha_y = 0.001\,\mathrm{m}^{-1}$), respectively. The spectral behaviour in the visible spectral range determined by the yellow substance absorption is well reproduced by SCIATRAN. The RMSE values between SCIATRAN simulations and measurements are $1.2 \cdot 10^{-2}$ and $1.5 \cdot 10^{-2}$, respectively, confirming a correct implementation of the stochastic model of a random mixture of ice particles and air gaps into SCIATRAN.

Melt ponds on sea ice

Melt ponds on sea ice are another surface type typical for high latitude regions.

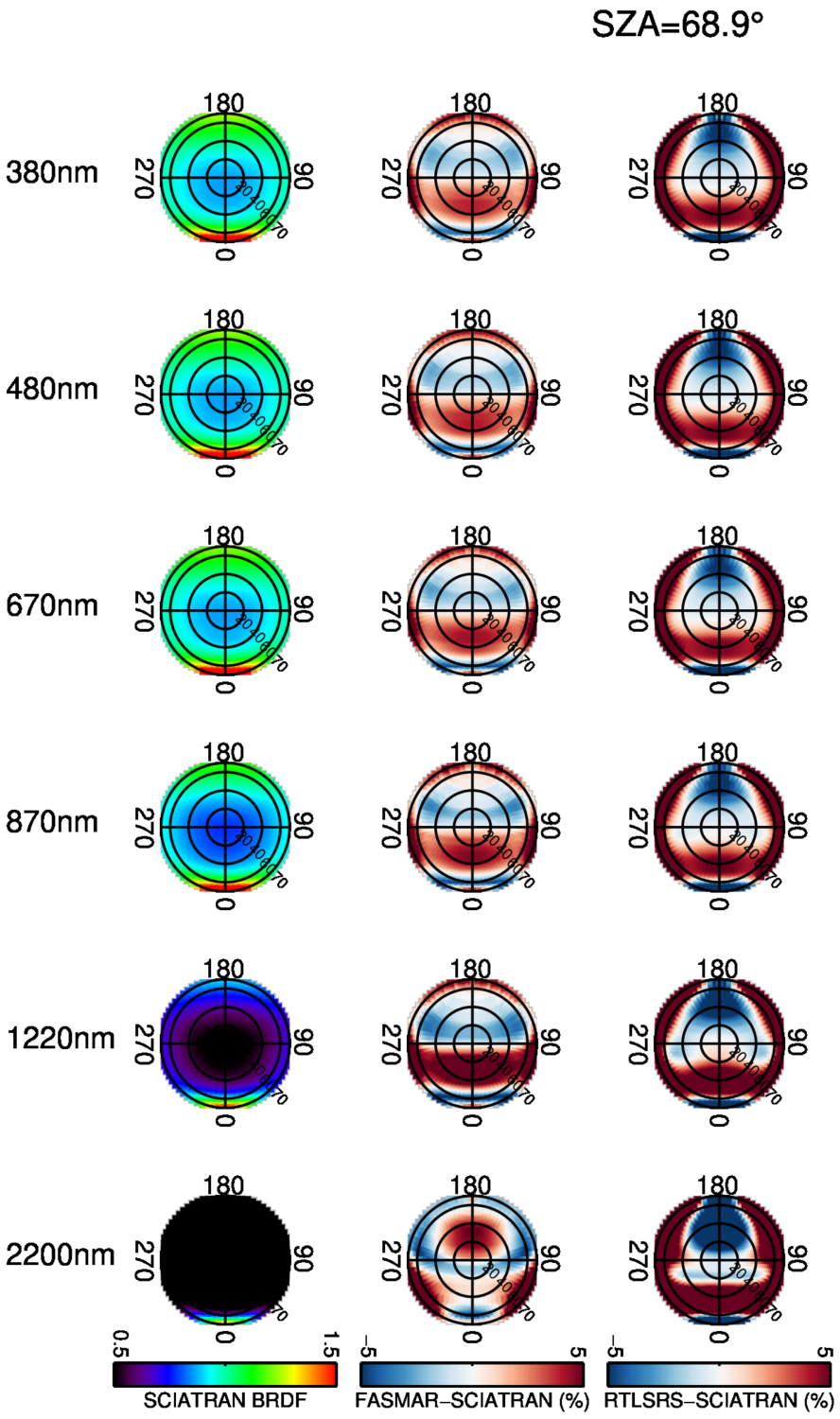

Figure 5: BRDF of the snow layer calculated using SCIATRAN and the difference between the results from FASMAR/RTLSRS models and SCIATRAN simulations for wavelengths of 380, 480 , 670 , 870, 1220, and 2200 nm and a solar zenith angle of 68.9°

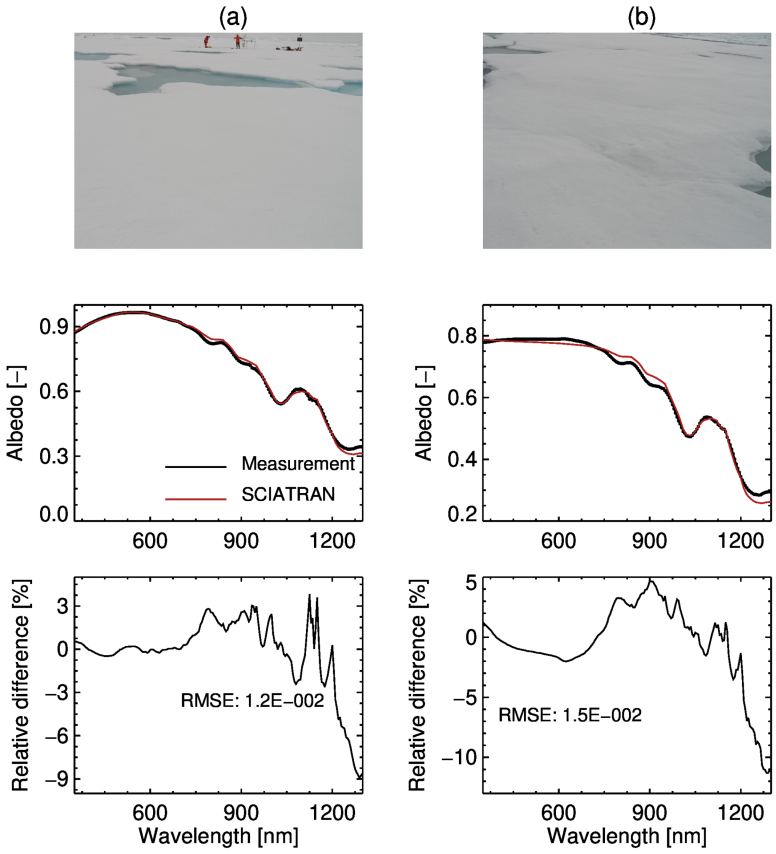

Figure 6: Comparisons of measured and simulated bright white ice spectral albedo corresponding to Figs. 8a and 8c in (Malinka et al., 2016). The upper row shows pictures of the measurements conditions, the middle row shows the measured and simulated spectral albedo, and the lower row shows the percentage difference between SCIATRAN simulations and campagin measurements.

Comparisons of SCIATRAN simulations for the spectral albedo of light-blue and dark open melt ponds with measurement data are shown in Fig. 7. Measurements of the spectral albedo were performed in the spectral range 300 - 2500 nm on August 2012 during a Polarstern cruise (Malinka et al., 2018). The examples presented in Fig. 7 were selected following Malinka et al. (2018). The spectral albedo of blue and dark melt ponds was measured under cloud-free and cloudy condition, respectively.

The simulations with SCIATRAN were performed using Eq. (29) of melt pond reflection described in Sect. 4.3.3 and aerosol-free atmosphere without gaseous absorption. The spectral albedo was calculated as a ratio of the reflected to the incident fluxes at the surface. For the blue pond, a cloud-free atmosphere was selected and the solar zenith angle was set in accordance with (Malinka et al., 2018) to 70°. For the dark pond, a water cloud with an optical thickness of 20, a geometrical thickness of 0.5 km, and a top height of 1.5 km was considered in addition.

Three parameters required to initialise the BRDF model in SCIATRAN (ice thickness, water depth and transport scattering coefficient) were obtained by fitting the simulated albedo with respect to the measured one within the spectral range 350 - 1350 nm. As pointed out by Malinka et al. (2018), measurements outside this spectral range show strong noise contamination. Therefore they were not used in the fitting process. The following parameters provide the minimum residual: ($H = 281.2\,\mathrm{cm}$, $z = 14.6\,\mathrm{cm}$, $\sigma_t = 2.08\,\mathrm{m}^{-1}$) and ($H = 23.7\,\mathrm{cm}$, $z = 42.8\,\mathrm{cm}$, $\sigma_t = 0.52\,\mathrm{m}^{-1}$) for the light-blue and dark melt ponds, respectively. It is seen from Fig. 7 that both spectral patterns and magnitudes of the spectral albedo agree well between the SCIATRAN simulations and the measurements, especially for the light-blue melt pond. As expected, the spectral albedo for the dark melt ponds is significantly lower than that for light-blue ones because of a much larger water depth. Typical spectral features can be seen for both scenes: 1) a higher albedo in the visible range and lower albedo in the infrared range; 2) a weak spectral dependence of the albedo in the NIR range. Both features above can be explained by the wavelength dependence of

the water absorption and Fresnel reflection at the air-water interface. Indeed, in contrast to the visible range, water absorbs a significant amount of radiation in the NIR so that a few centimetres thick layer of water completely absorbs radiation. This results in a saturation effect when a variation of the water absorption coefficient does not lead to a variation of the albedo and the wavelength dependence of the albedo is mainly determined by the spectral dependence of the Fresnel reflection.

The RMSE values between SCIATRAN simulations and measurements are $1.1 \cdot 10^{-2}$ and $3.8 \cdot 10^{-3}$ for the light-blue and dark melt ponds, respectively, confirming a correct implementation of the ice and melt ponds model in SCIATRAN.

7. Conclusions

This paper summarizes recent updates and new developments of aerosol, clouds and surface reflectance databases and models in the framework of the software package SCIATRAN. These updates and developments extend the capabilities of the radiative transfer modelling, especially by accounting for vertical inhomogeneties. Vertically inhomogeneous ice and mix-phase clouds as well as different aerosol types can be easily accounted for within SCIATRAN (V4.6). Additionally, widely used models and databases for the surface BRDF and albedo for different surface types (ocean, land, vegetation, snow, and melt pond on sea ice) are available with friendly user-interfaces. We believe that presented updates and new developments largely extend the application range of the SCIATRAN model in the field of the aerosol, cloud and surface remote sensing. The new implementations have been used or planned for use to support the development and generation of the XBAER global aerosol, cloud and surface data products. Users are advised to use the latest version of SCIATRAN capable of the new features described in this manuscript. The extended SCIATRAN version is freely available at the website of IUP, University of Bremen:

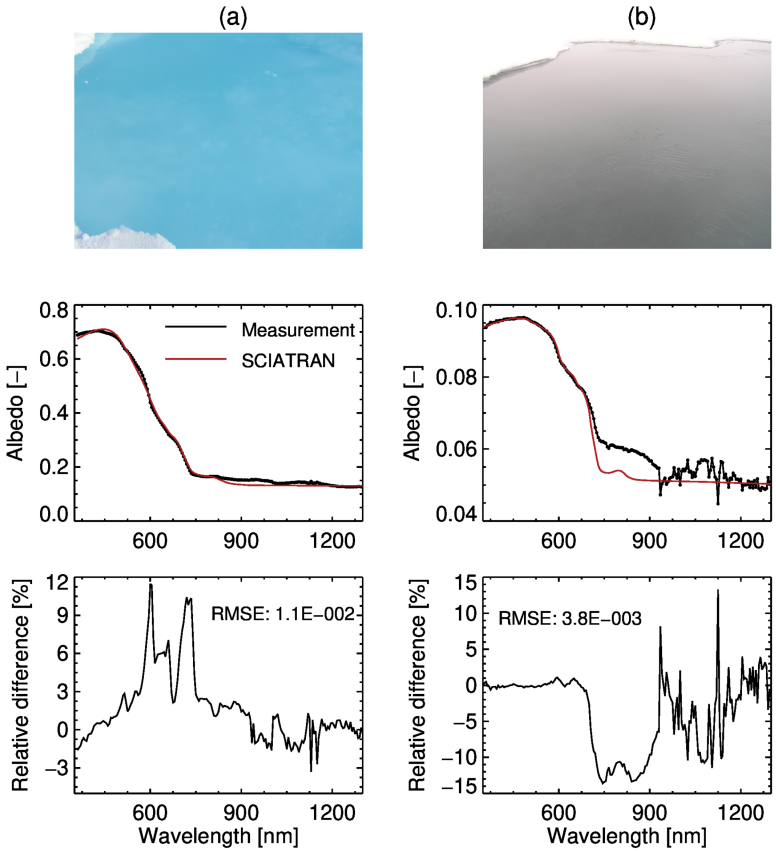

Figure 7: Comparisons of the spectral albedo for the light-blue (a) and dark (b) melt ponds corresponding to Fig. 6a and Fig. 8a in Malinka et al. (2018). The upper row shows pictures of the measurement scenes, the middle row shows the measured and simulated spectral albedo, and the lower row shows relative differences between the SCIATRAN simulations and campagin measurements.

http://www.iup.physik.uni-bremen.de/sciatran.

8. Code and data availability

The current version of SCIATRAN is available from the institution website: http://www.iup.physik.uni-bremen.de/sciatran under LGPL licence. The exact version of the model and input data used to produce the results used in this paper is archived on Zenodo (10.5281/zenodo.7376666)

9. Author contribution

LM and VR designed the experiments, LM, VR and AR developed the model code and performed the simulations. LM and VR prepared the manuscript with contributions from all co-authors. JB provided general oversight and guidance.

10. Competing interests

The contact author has declared that neither he nor the co-authors have any competing interests.

11. Acknowledgments

The valueable discussions with Dr. Robert Levy, Dr. Peter Colarco, Dr. Ping Yang, Dr. Bryan A. Baum, Dr. Masanori Saito, Dr. Oleg Dubovik and Dr. Aleksey Malinka are highly appreciated.

12. Financial support

This research was funded by the Deutsche Forschungsgemeinschaft (DFG, German Research Foundation) – Project-ID 268020496 – TRR 172.

Appendix A. Abbreviation

Appendix B. Land surface reflection models

RPV model includimg hot spot correction term.

One of the widely used models to approximate the bidirectional reflection function of a land surface is the so-called RPV model proposed by Rahman et al. (1993). In the framework of this model, the surface reflectance is parameterized by following expressions:

$$R(\mu_v, \mu_s, \varphi) \;=\; \rho_0 \Big[\mu_v\, \mu_s\, (\mu_v + \mu_s)\Big]^{k-1} F(g)\, H(G)\;, \tag{B.1}$$

$$F(g) \;=\; \frac{1-g^2}{(1+2g\cos\zeta+g^2)^{3/2}}\;,\quad H(G) = 1 \;+\; \frac{1-\rho_0}{1+G}\;, \tag{B.2}$$

$$G \;=\; \left[\tan^2\vartheta_v + \tan^2\vartheta_s + 2\tan\vartheta_s\tan\vartheta_v\cos\varphi_r\right]^{1/2}\;, \tag{B.3}$$

$$\cos\zeta \;=\; \mu_v\mu_s - \sqrt{(1-\mu_v^2)(1-\mu_s^2)}\,\cos\varphi_r\;, \tag{B.4}$$

where ρ_0 is the light reflection strength, k is the so-called Minnaert exponent, determining the reflection anisotropy level, and g is the asymmetry parameter controlling the relative amount of the forward and backward reflection, $\mu_v = \cos\vartheta_v$ and $\mu_s = \cos\vartheta_s$, with ϑ_v and ϑ_s denoting the viewing angle and the solar zenith angle, respectively, the phase angle, ζ, and the scattering angle, γ, are related as $\zeta = \pi - \gamma$. We note that ϑ_v and ϑ_s are defined as angles between the vertical z-axis direction and the direction to the satellite and to the sun, respectively. This means that ϑ_v and ϑ_s are always smaller than $\pi/2$, i.e., their cosines, μ_v and μ_s, are always positive. In contrast to the original publication of Rahman et al. (1993), the relative azimuthal angle, φ_r, is defined here to be zero for the forward scattering, i.e., if the observer looks toward the illumination source. Thus, the relative azimuth angle used by Rahman et al. (1993) differs by π from our definition. The function $H(G)$ describes the so-called hot spot effect seen in the measured data as a strong increase in the surface reflectance at $\vartheta_v = \vartheta_s$ and $\varphi_r = \pi$ (see, e.g., Hautecoeur and Leroy

Table A.7: Abbrevations used in this paper

Abbreviation	Full name
AATSR	Advanced Along-Track Scanning Radiometer
ACLOUD	Arctic Cloud Observations Using airborne measurements during polar Day
AERONET	Aerosol Robotic Network
AOT	Aerosol Optical Thickness
ART	Asymptotic Radiative Transfer
BC	Black Carbon
BRDF	Bidirectional Reflectance Distribution Function
CAS	Cloud, Aerosol and Surface
COT	Cloud Optical Thickness
CCI	Climate Change Initiative
C3S	Copernicus Climate Change Service
DT	Darket-Target
DU	DUst
EnMAP	Environmental Mapping and Analysis Program
EWT	Equivalent Water Thickness
FASMAR	Fast and Accurate Semi-analysical Model of Atmosphere-surface Reflectance
FOCAL	Fast atmOspheric traCe gAs retrievaL
FMF	Fine Mode Fraction
GOME	Global Ozone Monitoring Experiment
HSI	HyperSpectral Imager
IUP	Institute of Environmental Physics
LAI	Leaf Area Index
LAM	Leaf Mass per Area
MA	Moderately absorbing
MAN	Maritime Aerosol Network
MERIS	Medium Resolution Imaging Spectrometer
MERRA	Modern-Era Retrospective analysis for Research and Applications
MODIS	Moderate Resolution Imaging Spectroradiometer
MMR	Mass Mixing Ratio
NIR	Near InfRared
OC	Organic Carbon
OLCI	Ocean and Land Colour Instrument
OPAC	Optical Properties of Aerosols and Clouds
PARASOL	Polarization - Anisotropy of Reflectances for Atmospheric Sciences coupled with Observations from a Lidar
PROSAIL	PROspect+ SAIL
POLDER	POLarization and Directionality of the Earth's Reflectances
PSD	Particle Size Distribution
RH	Relative Humidity
RI	Refractive Index
RPV	Rahman-Pinty-Verstraete
RTLSR	RossThick-LiSparseReciprocal
RTLSRS	RossThick-LiSparseReciprocal-Snow
RMSE	Root-mean-square deviation
SA	Strongly absorbing
SAVI	Soil Adjusted Vegetation Index
SCIAMACHY	SCanning Imaging Absorption spectroMeter for Atmospheric CHartography
SGHM	Snow Grain Habit Mixture
SLSTR	Sea and Land Surface Temperature Radiometer
SRWSCD	Surface Reflectance Wavelength Shape Constrain Database
SS	Sea Salt
SSA	Single Scattering Albedo
SU	SUlfate
TOA	Top of the Atmosphere
UV	UltraViolet
VIS	VISible
WA	Weakly absorbing
WMO	World Meteorological Organization
XBAER	eXtensible Bremen Aerosol/cloud and surfacE parameters Retrieval

(1998)). In SCIATRAN, the RPV model is implemented using the land surface parameters (ρ_0, k, g) presented in Lyapustin (1999), allowing the user to account for BRDF of various reflecting surfaces such as the forest, savanna, plowed field, and others.

Kernel-based Ross-Li (RTLSR) model

The kernel-based linear Ross-Li BRDF model is implemented in SCIATRAN according to the following equation:

$$R(\mu_v, \mu_s, \varphi_r) \;=\; k_0 \;+\; k_v\, F_v(\mu_v, \mu_s, \varphi_r) \;+\; k_g\, F_g(\mu_v, \mu_s, \varphi_r)\,. \qquad \text{(B.5)}$$

Here, $F_v(\mu_v, \mu_s, \varphi_r)$ and $F_g(\mu_v, \mu_s, \varphi_r)$ represent the volume scattering and geometric-optic terms (or kernels), respectively, and k_0, k_g, and k_v are the input parameters. The geometric-optic kernel accounts for the mutual shadowing of protrusions (Maignan et al., 2004), and is implemented as follows:

$$\begin{aligned} F_g(\mu_v, \mu_s, \varphi_r) \;&=\; \frac{\mu_v + \mu_s}{\pi\, \mu_s\, \mu_v}\Big(t - \sin t\, \cos t - \pi\Big) \;+\; \frac{1 + \cos\zeta}{2\, \mu_s\, \mu_v}\,, \qquad \text{(B.6)} \\ \cos t \;&=\; \frac{2\, \mu_s\, \mu_v}{\mu_s + \mu_v}\sqrt{G^2 \;+\; (\tan\vartheta_s \tan\vartheta_v \sin\varphi_r)^2}\,, \\ t \;&=\; \begin{cases} \operatorname{acos} t\,, & \cos t \le 1 \\ 0\,, & \cos t > 1 \end{cases}\,, \end{aligned}$$

where G is given by Eq. (B.3).

The volume scattering term approximates the radiative transfer within a vegetation canopy and is calculated in accordance with the Roujean et al. (1992) model as

$$F_v(\mu_v, \mu_s, \varphi_r) \;=\; \frac{4\, C(\zeta, \zeta_0)}{3\,\pi(\mu_v + \mu_s)}\left[\left(\frac{\pi}{2} - \zeta\right)\cos\zeta + \sin\zeta\right] \;-\; \frac{1}{3}\,. \qquad \text{(B.7)}$$

Here, the phase angle ζ is given by Eq. (B.4) and the correction term $C(\zeta, \zeta_0)$ is used to improve the hot spot reflection modeling and it is implemented following Maignan et al. (2004) as

$$C(\zeta, \zeta_0) \;=\; 1 \;+\; \left(1 \;+\; \frac{\zeta}{\zeta_0}\right)^{-1}\,, \qquad \text{(B.8)}$$

where the parameter ζ_0 was found to be between $1-2^\circ$ for most of the reflecting land surfaces (Maignan et al., 2004).

Kernel-based Ross-Li vegetation-soil model

Following Breon and Vermote (2012), another representaion for the kernel-based linear Ross-Li model is implemented in SCIATRAN which allows one to introduce an alternative wavelength dependence of BRDF:

$$
\begin{aligned}
R_\lambda(\mu_v,\mu_s,\varphi_r) &= K_0(\lambda)\,\rho(\mu_v,\mu_s,\varphi_r)\,, \qquad \text{(B.9)}\\
\rho(\mu_v,\mu_s,\varphi_r) &= 1 \;+\; K_g F_g(\mu_v,\mu_s,\varphi_r) \;+\; K_v F_v(\mu_v,\mu_s,\varphi_r)\,,\\
K_0(\lambda) &= A_\lambda \left[\frac{2}{\pi}\int\limits_0^1\int\limits_0^1\int\limits_0^{2\pi} \rho(\mu_v,\mu_s,\varphi_r)\,\mu_v\mu_s d\mu_v d\mu_s d\varphi\right]^{-1}\,,\\
A_\lambda &= c\,A_{\rm veg}(\lambda) \;+\; (1-c)\,A_{\rm soil}(\lambda)\,,\\
K_v &= \alpha_v\,x \;+\; \beta_v\,, \quad K_g \;=\; \alpha_g\,x \;+\; \beta_g\,,\\
x &= (A_{\lambda_1}-A_{\lambda_2})/(A_{\lambda_1}+A_{\lambda_2})\,.
\end{aligned}
$$

Here, functions F_g and F_v are given by Eqs. (B.6) and (B.7), $A_{\rm veg}(\lambda)$ and $A_{\rm soil}(\lambda)$ are the spherical albedos of the vegetation and soil, respectively, c is a fraction of the vegetation, A_{λ_1} and A_{λ_2} are the spherical albedos of the vegetation-soil mixture at wavelengths $\lambda_1 = 865\,$nm and $\lambda_2 = 675\,$nm, respectively, and the parameters α_v, β_v, and α_g, β_g are given in Breon and Vermote (2012). Thus, the linear kernel-based soil-vegetation BRDF in SCIATRAN is initialized with the four input parameters, namely, spectral dependent Lambertian albedos of the soil, $A_{\rm soil}(\lambda)$, and vegetation, $A_{\rm veg}(\lambda)$, the vegetation fraction, c, in the vegetation-soil mixture, and the hot spot parameter ζ_0 (see Eq. (B.8)).

Modified RPV plus facet model

This BRDF model represents the surface reflectance as a sum of two components, i.e., a volumetric scattering term that is completely depolarizing and a

specular reflection term (Diner et al., 2012)

$$\mathbf{R}(\mu_v, \mu_s, \varphi_r) \;=\; \mathbf{R}_1(\mu_v, \mu_s, \varphi_r) + \mathbf{R}_2(\mu_v, \mu_s, \varphi_r)\;. \tag{B.10}$$

The modified Rahman-Pinty-Verstraete function (excluding the hot spot correction) is used for the volumetric term:

$$\mathbf{R}_1(\mu_v, \mu_s, \varphi_r) \;=\; \frac{\rho_0}{\pi}\left[(\mu_v + \mu_s)\mu_v\mu_s\right]^{k-1} e^{-b\cos\gamma}\,\mathbf{E}\;, \tag{B.11}$$

where ρ_0, k, and b are input parameters, γ is the scattering angle, the matrix $\mathbf{E}$ is a Mueller matrix with unity in the upper left-hand element and zeros everywhere else.

Second component is polarized and it represents the facet reflection like Cox and Munk ocean reflection model:

$$\mathbf{R}_2(\mu_v, \mu_s, \varphi_r) \;=\; C_2\,\frac{\mathcal{P}(\mu_n)\,S(\mu_v, \mu_s)}{4\mu_v\mu_s\mu_n}\,\mathbf{L}(-\alpha)\,\mathbf{F}(\gamma, m_r, m_i)\,\mathbf{L}(\alpha_0)\;, \tag{B.12}$$

where C_2 is a scaling parameter which defines the contribution of this component in the total reflection, $\mathcal{P}(\mu_n)$ is the facet slope probability distribution function, $S(\mu_v, \mu_s)$ is the shadowing factor, $\mathbf{L}(-\alpha)$ and $\mathbf{L}(\alpha_0)$ are rotation matrices, $\mathbf{F}(\gamma, m_r, m_i)$ is the Fresnel reflection matrix depending on the real m_r and imaginary m_i part of the surface refractive index. The user needs to define at desired wavelength grid the following model parameters: ρ_0, k, b and C_2, m_r, m_i.

Appendix C. White ice

The analytical expressions for the auxiliary function T_{dif}, average cosine g and absorption coefficient of the yellow substance α_y used in the white ice model described in Sect. 4.3.3 are given below following Malinka (2014, 2015) and Malinka et al. (2016).

The auxiliary function T_{dif} is defined as

$$T_{dif} = \frac{2(5n^6+8n^5+6n^4-5n^3-n-1)}{3(n^3+n^2+n+1)\,(n^4-1)} + \frac{n^2(n^2-1)^2}{(n^2+1)^3}\,\ln\frac{n+1}{n-1} - \frac{8n^4(n^4+1)}{(n^4-1)^2(n^2+1)}\,\ln n\,, \tag{C.1}$$

where n is the refractive index of water. The analytical expression for the average cosine g of the phase function is given by

$$g = \frac{1}{\omega}\left[r_1 + \frac{n^2\,t_1^2}{T_{dif}(1-n^2) - r_1 + n^4(1+\alpha\,a)}\right]\,, \tag{C.2}$$

where r_1 and t_1 are

$$r_1 = \frac{n(3n^{11}+3n^{10}+25n^9+25n^8+22n^7-282n^6+138n^5+186n^4+151n^3-89n^2+13n-3)}{24(n+1)\,(n^4-1)\,(n^2+1)^2} + \frac{8n^4(n^6-3n^4+n^2-1)}{(n^4-1)^2(n^2+1)^2}\,\ln n - \frac{(n^8+12n^6+54n^4-4n^2+1)(n^2-1)^2}{16(n^2+1)^4}\,\ln\frac{n+1}{n-1}\,, \tag{C.3}$$

$$t_1 = \frac{3n^8+3n^7-17n^6+55n^5-39n^4-7n^3-27n^2-11n-8}{24(n+1)\,(n^4-1)\,n} - \frac{(n^2-1)^4}{16(n^2+1)^2n}\,\ln\frac{n+1}{n-1} + \frac{4n^5}{(n^4-1)^2}\,\ln n\,. \tag{C.4}$$

The absorption coefficient of the yellow substance is given by

$$\alpha_y(\lambda) = \begin{cases} \alpha_y(\lambda_0)\,e^{-0.015\,(\lambda-\lambda_0)}\,, & \lambda \le 500\,\mathrm{nm} \\ \alpha_y(\lambda_0)\,e^{-0.015\,(500-\lambda_0)-0.011(\lambda-500)}\,, & \lambda > 500\,\mathrm{nm} \end{cases}\,, \tag{C.5}$$

where $\lambda_0 = 390\,\mathrm{nm}$ and $\alpha_y(\lambda_0)$ is the absorption coefficient of the yellow substance at the wavelength λ_0.

Appendix D. Melt ponds

The albedo of the under-pond ice layer needed by the melt pont model described in Sect. 4.3.3 is calculated according to the two-stream approximation developed by Zege et al. (1991):

$$A_b \;=\; A_0\,\frac{1-e^{-2\gamma\tau}}{1-A_0^2\,e^{-2\gamma\tau}}\,, \tag{D.1}$$

where $A_0 = 1 + t - \sqrt{t\,(t+2)}$ is the albedo of the semi-infinite layer with the same optical characteristics, $t = 8\,\alpha_i/3\,\sigma_t$, $\tau = (\sigma_t + \alpha_i)\,H$ is the layer optical thickness, H is its geometrical thickness, and γ is the asymptotic attenuation coefficient given by

$$\gamma = \frac{3}{4}\,\frac{\sigma_t}{\sigma_t + \alpha_i}\,\sqrt{t\,(t+2)}\,. \tag{D.2}$$

Here, α_i and σ_t are the ice absorption coefficient and transport scattering coefficient of ice (see, e.g., Chandrasekhar (1950)), respectively.

References

C. Arosio, A. Rozanov, E. Malinina, K.-U. Eichmann, T. von Clarmann, and J. P. Burrows. Retrieval of ozone profiles from OMPS limb scattering observations. *Atmospheric Measurement Techniques*, 11(4):2135–2149, 2018. doi: 10.5194/amt-11-2135-2018. URL `https://amt.copernicus.org/articles/11/2135/2018/`.

B. R. Barkstrom. A finite differencing method of solving anisotropic scattering problems. *J. Quant. Spectrosc. Radiat. Transfer*, 16:725–739, 1976.

B.A. Baum, P. Yang, A.J. Heymsfield, S. Platnick, M.D. King, and S.T. Bedka. Bulk scattering models for the remote sensing of ice clouds Part II: Narrowband models. *J. Appl. Meteor.*, 44:1896–1911, 2005.

B.A. Baum, P. Yang, A.J. Heymsfield, C.G. Schmitt, Y. Xie, and A. Bansemer. Improvements in shortwave bulk scattering and absorption models for the remote sensing of ice clouds. *J. Appl. Meteorol. Climatol.*, 50:1037 – 1056, 2011.

H.J. Bolle. A preliminary cloudless stardard atmosphere for radiation computation, wcp-112. *World Meteorological Organization*, 1986.

H. Bovensmann, M. Buchwitz, J. P. Burrows, M. Reuter, T. Krings, K. Gerilowski, O. Schneising, J. Heymann, A. Tretner, and J. Erzinger. A remote sensing technique for global monitoring of power plant CO_2 emissions from space and related applications. *Atmospheric Measurement Techniques*, 3(4):781–811, 2010. doi: 10.5194/amt-3-781-2010. URL `https://amt.copernicus.org/articles/3/781/2010/`.

F.M. Breon and E. Vermote. Correction of MODIS surface reflectance time series for BRDF effects. *Remote Sensing of Environment*, 125:1–9, 2012.

M. Buchwitz, M. Reuter, H. Bovensmann, D. Pillai, J. Heymann, O. Schneising, V. Rozanov, T. Krings, J. P. Burrows, H. Boesch, C. Gerbig, Y. Mei-

jer, and A. Löscher. Carbon monitoring satellite (CarbonSat): assessment of atmospheric CO_2 and CH_4 retrieval errors by error parameterization. *Atmospheric Measurement Techniques*, 6(12):3477–3500, 2013. doi: 10.5194/amt-6-3477-2013. URL `https://amt.copernicus.org/articles/6/3477/2013/`.

J. P. Burrows, E. Holzle, A. P. H. Goede, H. Visser, and W. Fricke. Sciamachy - scanning imaging absorption spectrometer for atmospheric chartography. *Acta Astronautica*, 35(7):445–451, 1995.

S. Chandrasekhar. *Radiative transfer*. London: Oxford University Press, 1950.

M. Degunther and R. Meerkotter. Influence of inhomogeneous surface albedo on uv irradiance: effect of a stratus cloud. *Journal of Geophysical Research*, 105:D18, 2000.

David J. Diner, Feng Xu, John V. Martonchik, Brian E. Rheingans, Sven Geier, Veljko M. Jovanovic, Ab Davis, Russell A. Chipman, and Stephen C. McClain. Exploration of a Polarized Surface Bidirectional Reflectance model using the ground-based multiangle spectropolarimetric imager. *Atmosphere*, 3(4):591–619, 2012. ISSN 2073-4433. doi: 10.3390/atmos3040591. URL `https://www.mdpi.com/2073-4433/3/4/591`.

O. Dubovik, A. Sinyuk, T. Lapyonok, B. N. Holben, M. Mischchenko, P. Yang, T. F. Eck, H. Volten, O. Munoz, B. Veihelmann, W. J. van der Zande, J. F. Leon, M. Sorokin, and I. Slutsker. Application of spheroid models to account for aerosol particle nonsphericity in remote sensing of desert dust. *Journal of Geophysical Rsearch : Atmospheres*, 111:D11, 2006.

O. Dubovik, T. Lapyonok, P. Litvinov, M. Herman, D. Fuertes, F. Ducos, A. Lopatin, A. Chaikovksy, B. Torres, Y. Derimain, X. Huang, M. Aspetsberger, and C. Federspiel. Grasp: a versatile algorithm for characterizing the atmosphere. *SPIE News-room*, 2014. doi: 10.1117/2.1201408.005558.

E. M. Feigelson, editor. *Radiation in cloudy atmosphere*. Gidrometeoizdat (in Russian), Leningrad, 1981.

K. Gerilowski, A. Tretner, T. Krings, M. Buchwitz, P. P. Bertagnolio, F. Belemezov, J. Erzinger, J. P. Burrows, and H. Bovensmann. Mamap – a new spectrometer system for column-averaged methane and carbon dioxide observations from aircraft: instrument description and performance analysis. *Atmos. Meas. Tech.*, 4:215–243, 2011.

I. E. Gordon, L. S. Hargreaves, R. J. Hashemi, and et al. The hitran2020 molecular spectroscopic database. *J. Quant. Spectrosc. Radiat. Transf.*, 277: 107949, 2022.

O. Hautecoeur and M. M. Leroy. Surface bidirectional reflectance distribution function observed at global scale by POLDER/ADEOS. *Geoph. Res. Letters*, 25(22):4197–4200, 1998.

M. Hess, P. Köpke, and I. Schult. Optical properties of aerosols and clouds: The software package OPAC. *Bulletin of the American Meteorological Socie*, 79:831–844, 1998.

S. Jacquemound, W. Verhoef, F. Baret, C. Bacour, P.J. Zarco-Tejade, G. P. Asner, C. Francois, and S. L. Ustin. Prospect + sail models : A review of use for vegetation characterization. *Remote sensing of environment*, 113:S56 – S66, 2009.

E. Jarvinen, E. Jourdan, D. Neubauer, B. Yao, C. Liu, M.O. Andreae, U. Lohmann, M. Wendisch, G. M. McFarquhar, T. Leisner, and M. Schnaiter. Additional global climate colling by clouds due to ice crystal complexity. *Atmospheric Chemistry and Physics*, 18:15767 – 15781, 2018.

Z.T. Jiao, A Ding, A. Kokhanvosky, C. Schaaf, F.-M. Bréon, Y. Dong, Z. Wang, Y. Liu, X. Zhang, S. Yin, L. Cui, L. Mei, and Y. Chang. Development of a snow kernel to better model the anisotropic reflectance of pure snow in a

kernel-driven BRDF model framework. *Remote Sensing of Environment*, 221: 198–209, 2019.

M.D. King, S. Platnick, W.P. Menzel, S.A. Ackerman, and P.A. Hubanks. Spatial and temporal distribution of clouds observed by modis onboard the terra and aqua satellites. *IEEE Transactions on Geoscience and Remote Sensing*, 51:3826 – 3852, 2013.

A. A. Kokhanovsky. Reflection of light from particulate media with irregularly shaped particles. *Journal of Quantitative Spectroscopy and Radiative Transfer*, 96:1–10, 2005.

A. A. Kokhanovsky. Cloud optics. *Dordrecht: Springer*, 1:1–276, 2006.

A. A. Kokhanovsky and V. V. Rozanov. Droplet vertical sizing in warm clouds using passive optical measurements from a satellite. *Atmos. Meas. Tech.*, 5 (3):517–528, 2012.

A. A. Kokhanovsky and E. P. Zege. Scattering optics of snow. *Applied Optics*, 43:1589–1602, 2004.

P. Köpke, J. Gasteiger, and M. Hess. Technical Note: Optical properties of desert aerosol with non-spherical mineral particles: data incorporated to OPAC. *Atmos. Chem. Phys.*, 15:5947–5956, 2015.

G.A. Korn and T.M. Korn. Mathematical handbook for scientists and engineers. *New York, San Francisco, Toronto, London, Sydney: McGraw-Hill Book Company*, pages 1–1154, 1968.

L. Lelli, V. V. Rozanov, M. Vountas, and J. P. Burrows. Polarized radiative transfer through terrestrial atmosphere accounting for rotational raman scattering. *Journal of Quantitative Spectroscopy and Radiative Transfer*, 200: 70–89, 2017.

C. Levoni, M. Cervino, R. Guzzi, and F. Torricella. Atmospheric aerosol optical properties: a database of radiative characteristics for different components and classes. *Apppl. Opt.*, 36:8031 – 8041, 1997.

R. C. Levy, L. A. Remer, and O. Dubovik. Global aerosol optical properties and application to Moderate Resolution Imaging Spectroradiometer aerosol retrieval over land. *Journal of Geophysical Research*, 112:D13210, 2007.

R. C. Levy, S. Mattoo, L. A. Munchak, L. A. Remer, A. M. Sayer, F. Patadia, and N. C. Hsu. The collection 6 modis aerosol products over land and ocean. *Atmospheric Measurement Techniques*, 6:2989–3034, 2013.

W. Lucht, C. B. Schaaf, and A. H. Strahler. An algorithm for the retrieval of albedo from space using semiempirical BRDF models. *IEEE TRANSACTIONS ON GEOSCIENCE AND REMOTE SENSING*, 38:977–998, 2000.

A. I. Lyapustin. Atmospheric and geometrical effects on land surface albedo. *J. Geophys. Res.*, 104(D4):4127–4143, 1999.

A. Macke, J. Mueller, and E. Raschke. Scattering properties of atmospheric ice crystals. *J. Atmos. Sci.*, 53:2813–25, 1996.

F. Maignan, F. M. Breon, and R. Lacaze. Bidirectional refletance of earth targets: evaluation of analytical models using a large set of space-borne measurements with emphasis on the hot spot. *Remote Sensing of Environment*, 90:210–20, 2004.

A. Malinka. Analytical expressions for characteristics of light scattering by arbitrarily shaped particles in the wkb approximation. *J. Opt. Soc. Am. A*, 32:1344–1351, 2015.

A. Malinka, E. Zege, G. Heygster, and L. Istomina. Reflective properties of white sea ice and snow. *The Cryosphere*, 10:2541–2557, 2016. doi: https://doi.org/10.5194/tc-10-2541-2016.

A. Malinka, E. Zege, L. Istomina, G. Heygster, G. Spreen, D. Perovich, and C. Polashenski. Reflective properties of melt ponds on sea ice. *The Cryosphere*, 12:1921 – 1937, 2018.

A. V. Malinka. Light scattering in porous materials: Geometrical optics and stereological approach. *Journal of Quantitative Spectroscopy and Radiative Transfer*, 141:14–23, 2014.

E. Matthews. Global vegetation and land use: new high resolution databases for climate studies. *J. Clim. Appl. Meteorol.*, 22:474–87, 1983.

L. Mei, V. Rozanov, M. Vountas, J. P. Burrows, R. C. Levy, and W. Lotz. Retrieval of aerosol optical properties using MERIS observations: Algorithm and some first results. *Remote Sensing of Environment*, 197:125–140, 2017a.

L. Mei, M. Vountas, L. Gómez-Chova, V. Rozanov, M. Jäger, W. Lotz, J.P. Burrows, and R. Hollmann. A cloud masking algorithm for the XBAER aerosol retrieval using MERIS data. *Remote Sensing of Environment*, 197: 141–160, 2017b.

L. Mei, V. Rozanov, M. Vountas, and J.P. Burrows. The retrieval of ice cloud parameters from multi-spectral satellite observations of reflectance using a modified XBAER algorithm. *Remote Sensing of Environment*, 215:128–144, 2018a.

L. Mei, V. Rozanov, M. Vountas, J.P. Burrows, and A. Richter. Xbaer-derived aerosol optical thickness from olci/sentinel-3 observation. *Atmospheric Chemistry and Physics*, 18:2511–2523, 2018b.

L. Mei, V. Rozanov, H. Jethva, K. G Meyer, L. Lelli, M. Vountas, and J.P. Burrows. Extending xbaer algorithm to aerosol and cloud condition. *IEEE Transactions on Geoscience and Remote Sensing*, 57:1–14, 2019.

L. Mei, S. Vandenbussche, V. Rozanov, E. Proestakis, V. Amiridis, S. Callewaert, M. Vountas, and J.P. Burrows. On the retrieval of aerosol optical depth over cryosphere using passive remote sensing. *Remote sensing of Environment*, 241:111731, 2020a.

L. Mei, V. Rozanov, C. Ritter, B. Heinold, Z. Jiao, M. Vountas, and J. P. Burrows. Retrieval of aerosol optical thickness in the Arctic snow-covered

regions using passive remote sensing: Impact of aerosol typing and surface reflection model. *IEEE Transactions on Geoscience and Remote Sensing*, 58: 5117–5131, 2020b.

L. Mei, V. Rozanov, C. Pohl, M. Vountas, and J. P. Burrows. The retrieval of snow properties from SLSTR/Sentinel-3 – part 1: method description and sensitivity study. *The Cryosphere*, pages 1–45, 2021a. doi: 10.5194/tc-2020-269. URL `https://tc.copernicus.org/preprints/tc-2020-269/`.

L. Mei, V. Rozanov, E. Jäkel, X. Cheng, M. Vountas, and J. P. Burrows. The retreival of snow properties from SLSTR/Sentinel-3 – part 2: results and validation. *The Cryosphere*, pages 1–41, 2021b. doi: 10.5194/tc-2020-270. URL `https://tc.copernicus.org/preprints/tc-2020-270/`.

L. Mei, V. Rozanov, Z. Jiao, and J. P. Burrows. A new snow bidirectional reflectance distribution function model in spectral regions from UV to SWIR: model development and application to ground-based, aircraft and satellite observations. *ISPRS Journal of Photogrammetry and Remote Sensing*, 188: 269–285, 2022.

M. I. Mishchenko. Radiation force caused by scattering, absorption, and emission of light by nonspherical particles. *Journal of quantitative spectroscopy and radiative transfer*, 70:811 – 816, 2001.

M.I. Mishchenko, J. M. Dlugach, E.G. Yanvitskij, and N. T. Zakharova. Bidirectional reflectance of flat, optically thick particulate layers: an efficient radiative transfer solution and applications to snow and soil surface. *Journal of quantitative spectroscopy and radiative transfer*, 63:409 – 432, 1999.

S. Noël, K. Weigel, K. Bramstedt, A. Rozanov, M. Weber, H. Bovensmann, and J. P. Burrows. Water vapour and methane coupling in the stratosphere observed using SCIAMACHY solar occultation measurements. *Atmospheric Chemistry and Physics*, 18(7):4463–4476, 2018. doi: 10.5194/acp-18-4463-2018. URL `https://acp.copernicus.org/articles/18/4463/2018/`.

S. Platnick, K. G. Meyer, M. D. King, G. Wind, N. Amarasinghe, B. Marchant, G. T. Arnold, Z. Zhang, P. A. Hubanks, R.E. Holz, P. Yang, W. L. Ridgway, and J. Riedi. The modis cloud optical and mircophysical products: Collection 6 updates and examples from terra and aqua. *IEEE Trans. Geosci. Remote Sens.*, 55:502 – 525, 2017.

C. Pohl, V. V. Rozanov, L. Mei, J. P. Burrows, G. Heygster, and G. Spreen. Implementation of an ice crystal single-scattering property database in the radiative transfer model SCIATRAN. *Journal of Quantitative Spectroscopy and Radiative Transfer*, 253:107118, 2020.

H. Rahman, B. Pinty, and M.M. Verstraete. Coupled surface-atmosphere reflectance (CSAR) model 2. Semiempirical surface model usable with NOAA advanced very high resolution radiometer data. *Journal of Geophysical Research*, 98:20791–20801, 1993.

C.A. Randles, A.M. da Silva, P. R. Colarco V. Buchard, A. Darmenov, R. Govindaraju, A. Smirnov, B. Holben, R. Ferrare, J. Hair, Y. Shinozuka, and C. J. Flynn. The merra-2 aerosol reanalysis, 1980 onward. part 1: System description and data assimilation evaluation. *Journal of Climate*, 30:6823 – 6850, 2017.

L. A. Remer, Y.J. Kufman, D. Tanre, S. Mattoo, D.A. Chu, J.V. Martins, R.R. Li, C. Ichoku, R.C. Levy, R.G. Kleidman, T.F. Eck, E. Vermote, and B.N. Holben. The MODIS aerosol algorithm, products and validation. *Journal of the atmospheric sciences*, 62:947–973, 2005.

L. A. Remer, R.C. Levy, S. Mattoo, D. Tanre, P. Gupta, Y. Shi, V. Sawyer, L. A. Munchak, Y. P. Zhou, M. Kim, C. Ichoku, F. Patadia, R. R. Li, S. Gasso, R. G. Kleidman, and B. N. Holben. The dark target algorithm for observing the global aerosol system: Past, present , and future. *Remote sensing*, 12: 2900, 2020.

M. Reuter, M. Buchwitz, O. Schneising, S. Noël, V. Rozanov, H. Bovensmann, and J.P. Burrows. A fast atmospheric trace gas retrieval for hyperspectral

instruments approximating multiple scattering—part 1: Radiative transfer and a potential oco-2 xco2 retrieval setup. *Remote Sens.*, 9:1159, 2017.

A. Richter, J.P. Burrows, H. Nuess, C. Granier, and U. Niemeier. Increase in tropospheric nitrogen dioxide over China observed from space. *Nature*, 437: 129–132, 2005.

J. L. Roujean, M. Leroy, and P. Y. Deschamps. A bidirectional reflectance model of the Earth's surface for the correction of remote sensing data. *J. Geophys. Res. Atmos.*, 97:20455–20468, 1992.

A. Rozanov, V. Rozanov, and J. P. Burrows. Combined differential-integral approach for the radiation field computation in a spherical shell atmosphere : Nonlimb geometry. *J. Geophys. Res.*, 105(D18):22937 – 22942, 2000. doi: https://doi.org/10.1029/2000JD900378.

A. Rozanov, V. Rozanov, and J. P. Burrows. A numerical radiative transfer model for a spherical planetary atmosphere: combined differential-integral approach involving the Picard iterative approximation. *J. Quant. Spectrosc. Radiat. Transfer*, 69(4):491–512, 2001. doi: 10.1016/S0022-4073(00)00100-X.

A. Rozanov, V. V. Rozanov, M. Buchwitz, A. Kokhanovsky, and J. P. Burrows. Sciatran 2 - a new radiative transfer model for geophysical applications in the 175 - 2400 nm spectral region: the pseudo-spherical version. *Adv. Space Res.*, 36:1015–9, 2005.

A. Rozanov, V. V. Rozanov, and J. P. Burrows. Modeling of inelastically scattered radiation: Rotational raman scattering in the spherical earth's atmosphere. *Journal of Quantitative Spectroscopy and Radiative Transfer*, 268: 107611, 2021.

A. Rozanov, V. Rozanov, and L. Mei. Radiative transfer model sciatran v4.6: source code and required data base. *Zenodo*, page https://doi.org/10.5281/zenodo.7376666, 2022.

V. V. Rozanov and M. Vountas. Radiative transfer equation accounting for rotational raman scattering and its solution by the discrete-ordinates method. *Journal of Quantitative Spectroscopy and Radiative Transfer*, 133:603–618, 2013.

V. V. Rozanov, D. Diebel, R.J.D. Spurr, and J. P. Burrows. Gometran: a radiative transfer model for the satellite project gome, the plane-parallel version. *J. Geophys. Res.*, 102:16683–95, 1997.

V. V. Rozanov, M. Buchwitz, K.-U. Eichmann, R. de Beek, and J. P. Burrows. Sciatran - a new radiative transfer model for geophysical applications in the 240 - 2400 nm spectral region: the pseudo-spherical version. *Adv. Space Res.*, 29:1831–5, 2002.

V. V. Rozanov, A. V. Rozanov, A. A. Kokhanovsky, and J. P. Burrows. Radiative transfer through terrestrial atmosphere and ocean: software package SCIATRAN. *J. Quant. Spectr. Radiat. Transfer*, 133:13–71, 2014. doi: 10.1016/j.jqsrt.2013.07.004.

V. V. Rozanov, T. Dinter, A. V. Rozanov, A. Wolanin, A. Bracher, and J. P. Burrows. Radiative transfer modeling through terrestrial atmosphere and ocean accounting for inelastic processes: Software package SCIATRAN. *Journal of Quantitative Spectroscopy and Radiative Transfer*, 194:65–85, 2017.

M. Saito, P. Yang, N. G. Loeb, and S. Kato. A novel parameterization of snow albedo based on a two-layer snow model with a mixture of grain habits. *J. Atmos. Sci.*, 76:1419–1436, 2019.

D. Segelstein. The complex refractive index of water. *Master thesis*, University of Missouri, 1981.

C. E. Siewert. A discrete-ordinates solution for radiative-transfer models that include polarization effects. *J. Quant. Spectr. Radiat. Transfer*, 64:227–254, 2000.

B. M. Sinnhuber, N. Sheode, M. Sinnhuber, M.P. Chipperfield, and W. Feng. The contribution of anthropogenic bromine emissions to past stratospheric ozone trends: a modelling study. *Atmos. Chem. Phys.*, 9:2863 – 2871, 2009.

A. Smirnov, B.N. Holben, I. Slutsker, D. M. Giles, C. R McClain, T. F. Eck, S. M. Sakerin, A. Macke, P. Croot, G. Zibordi, P. K. Quinn, J. Sciare, S. Kinne, M. Harvey, T. J. Smyth, S. Piketh, T. Zielinkski, A. Proshutinsky, J. I. Goes, N. B. Nelson, P. Larouche, V. F. Radionov, P. Goloub, K. Krishna Moorthy, R. Matarrese, E. J. Robertson, and F. Jourdin. Maritime aerosol network as a component of aerosol robotic network. *Journal of Geophysical Research*, 114:D06204, 2009.

V. V. Sobolev. *Light Scattering in Planetary Atmospheres.* Nauka, Moscow, 1972.

M. Weber, M. Coldewey-Egbers, V. E. Fioletov, S. M. Frith, J. D. Wild, J. P. Burrows, C. S. Long, and D. Loyola. Total ozone trends from 1979 to 2016 derived from five merged observational datasets – the emergence into ozone recovery. *Atmospheric Chemistry and Physics*, 18(3):2097–2117, 2018. doi: 10.5194/acp-18-2097-2018. URL `https://acp.copernicus.org/articles/18/2097/2018/`.

A. Wolanin, V. V. Rozanov, T. Dinter, S. Noël, M. Vountas, J. P. Burrows, and A. Bracher. Global retrieval of marine and terrestrial chlorophyll fluorescence at its red peak using hyperspectral top of atmosphere radiance measurements: Feasibility study and first results. *Remote Sensing of Environment*, 166:243 – 261, 2015.

P. Yang, L. Bi, B. A. Baum, K-N. Liou, G.W. Kattawar, M.I. Mishchenko, and B. Cole. Spectrally consistent scattering, absorption, and polarization properties of atmospheric ice crystals at wavelengths from 200 to 100000 nm. *Journal ofAtmospheric Sciences*, 70:330–347, 2013.

E. P. Zege, A. P. Ivanov, and I. L. Katsev. Image transfer through a scattering medium. *Springer-Verlag Berli Heidelberg*, 1:349, 1991.

1435 T. X. P. Zhao, I. Laszlo, O. Dubovik, B. N. Holben, J. Sapper, D. tanre, and C. pietras. A study of the effect of non-spherical dust particles on the avhrr aerosol optical thickness retrievals. *Journal of quantitative spectroscopy and radiative transfer*, 30:1317, 2003.